

Benchmarking the readout of a superconducting qubit for repeated measurements

S. Hazra,^{1,*} W. Dai,^{1,*} T. Connolly,¹ P. D. Kurilovich,¹ Z. Wang,¹ L. Frunzio,¹ and M. H. Devoret^{1,†}

¹*Department of Applied Physics, Yale University, New Haven, Connecticut 06520, USA
and Yale Quantum Institute, Yale University, New Haven, Connecticut 06520, USA*

(Dated: July 16, 2024)

Readout of superconducting qubits faces a trade-off between measurement speed and unwanted back-action on the qubit caused by the readout drive, such as T_1 degradation and leakage out of the computational subspace. The readout is typically benchmarked by integrating the readout signal and choosing a binary threshold to extract the “readout fidelity”. We show that such a characterization may significantly overlook readout-induced leakage errors. We introduce a method to quantitatively assess this error by repeatedly executing a composite operation—a readout preceded by a randomized qubit-flip. We apply this technique to characterize the dispersive readout of an intrinsically Purcell-protected qubit. We report a binary readout fidelity of 99.63% and quantum non-demolition (QND) fidelity exceeding 99.00% which takes into account a leakage error rate of $0.12 \pm 0.03\%$, under a repetition rate of $(380\text{ns})^{-1}$ for the composite operation.

Fast and accurate single-shot qubit readout is crucial for a multitude of quantum computing experiments including, measurement-based state preparation [1], entanglement generation [2–4] and quantum error correction (QEC) [5–10]. Recent advancements in superconducting qubit readout coupled with near-quantum-limited measurement efficiency have made it possible to demonstrate quantum error correction with both surface code [8, 9] and bosonic codes [5–7]. In these experiments, efficient entropy removal from the quantum system is achieved by repeated application of high fidelity readout and reset of the physical ancilla qubits. A quantum non-demolition (QND) measurement [11] perfectly correlates the post-readout state of the qubit with the readout outcome, alleviating the need for unconditional reset [12] of the ancilla. A purely dispersive interaction between a qubit and its readout resonator would yield a QND readout scheme. In reality, this interaction is approximately realized in superconducting circuits [13] when an artificial atom is linearly coupled to the readout resonator. The linear hybridization of the qubit and the readout resonator leads to Purcell decay of the qubit. This prevents arbitrary increase of the qubit-resonator dispersive interaction χ_{qr} and the external coupling rate of the resonator κ_r , which sets a maximum speed of the readout for a given power. Moreover, at higher readout power, the dispersive approximation breaks down [14], causing readout-induced leakage [15, 16] into the non-computational states of the physical qubit. These limitations prohibit the simultaneous pursuit of the readout speed, fidelity and QND-ness.

In QEC, entangling operations and ancilla readouts are repeated, as illustrated in Fig.1. The readout-induced leakage errors can leave the ancilla in undesirable highly-excited states for multiple cycles, and can also spread into neighbouring qubits [17]. Thus, even a small leakage probability poses a greater threat compared to discrimination error or Pauli error. Often, the “readout fidelity” [1, 18–23] extracted from the *binary-thresholded* outcomes is used as the only metric to experimentally

optimize the readout parameters. While such a metric is sufficient to quantify the Pauli error (occurring during the readout process) and the discrimination error, it fails to faithfully identify readout-induced leakage, especially if the latter occurs with a low probability compared to other readout errors. The standard measure of QND-ness as the correlation of two successive binary readout outcomes [21–23] also overlooks leakage when the readout outcomes of the leakage states predominantly fall on one side of the threshold. Therefore, such methods do not reflect the true character of the repeated readout operations. Is there a complete way to benchmark the readout operation with binary outcome?

In this Letter, we demonstrate a novel readout benchmarking technique, “pseudo-syndrome detection”, where we mimic a syndrome detection cycle in QEC by repeating a composite operation—a readout preceded by a random qubit flip. This method offers a faithful characterization of the readout under repeated implementations and provides an accurate estimation of the readout QND-ness. We perform the dispersive readout on a Purcell-protected transmon. We optimize the readout pulses

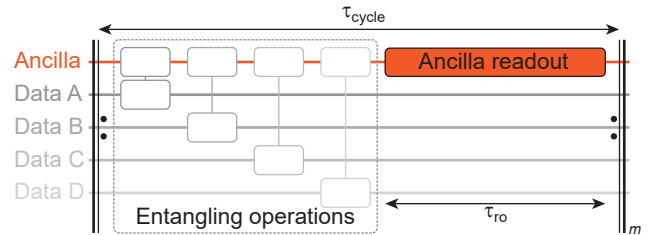


Figure 1. A syndrome detection cycle in QEC. Each cycle consists of an ancilla readout preceded by entangling operations with data qubits, mapping the syndrome onto the ancilla. We characterize the readout performance by mimicking this experiment on a single ancilla, with the “syndrome” artificially generated by randomly applying identity and bit-flip operations.

(frequency, envelope and duration) to achieve maximum fidelity for a set of different readout powers. Then we characterize leakage error for these readout pulses with our technique. We show that readouts with nominally identical fidelities can have leakage probability differing by more than one order of magnitude. This demonstrates that a faithful characterization of the readout-induced leakage should be a necessary step in optimizing the performance of quantum processors.

Qubit with intrinsic Purcell-protection.—To eliminate the radiative decay of the qubit we design a symmetric two-mode Josephson device—termed “dimon”—that benefits from intrinsic Purcell protection [22, 24–27]. As illustrated in Fig. 2(a), the device (white), is symmetrically placed at the center of a 3D rectangular cavity (dark grey), functioning as the readout resonator. The resonator is aperture-coupled to a waveguide filter mode (shown in pink) that strongly emits into a transmission line. The system can be modelled by the lumped-element circuit [28] shown in Fig. 2(c). We adopt such a coupling scheme to minimize parasitic coupling of the dimon to the transmission line. The bilateral symmetry of the dimon ensures that the two normal modes of the circuit are dipolar and quadrupolar in nature, respectively. The dipolar mode undergoes hybridization with the readout resonator through conventional charge-charge linear coupling [29], whereas the quadrupolar mode has no linear coupling with the readout resonator. We designate the quadrupolar mode as the ‘qubit’, and the dipolar mode as the ‘mediator’. The two dimon modes interact via a strong purely non-linear coupling that leads to a *mediated* dispersive interaction between the qubit and the readout resonator, despite having no linear hybridization between the two. To the leading order, this mediated dispersive shift, $\chi_{qr} = g_{mr}^2 \chi_{qm} / [\Delta_{mr}(\Delta_{mr} + \chi_{qm})]$ depends on the qubit-mediator cross-Kerr interaction χ_{qm} , mediator-readout detuning Δ_{mr} , and their linear coupling strength g_{mr} . The absence of linear hybridization of the qubit with the readout resonator makes it inherently protected against Purcell decay across all frequencies. Thus, the Purcell protection is robust against Stark shifts induced by all the drives, including the readout drive itself.

Device parameters.—Our experimental device has a total qubit-resonator dispersive shift $\chi_{qr}/2\pi = -6.4$ MHz and the external coupling rate of the readout resonator via the waveguide coupler is set to $\kappa_r/2\pi = 11.6$ MHz, enabling fast readout. The details of the device parameters are provided in the supplemental materials [30]. To quantify the Purcell decay rate of the qubit through this strongly coupled port (S, shown in maroon in Fig. 2(a)), we first drive Rabi oscillations on the qubit and mediator modes from port S. The ratio of drive powers at port S to achieve the same Rabi rate, $P_q/P_m = 40$ dB is related to the Purcell T_1 of the two modes by $(T_{1,q}^P/T_{1,m}^P) = (P_q\omega_m/P_m\omega_q)$ [23]. We then measure

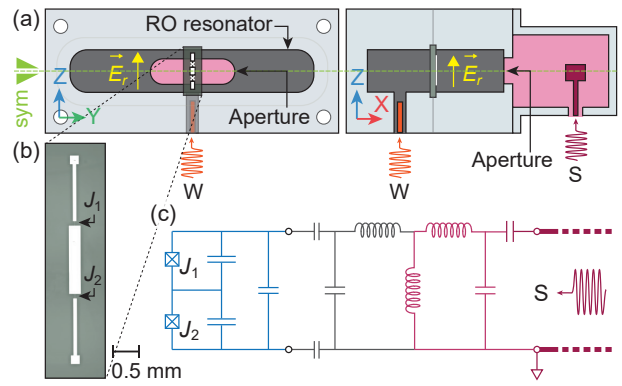


Figure 2. Experimental device. (a) Schematic of the physical realization of dimon in the 3D architecture viewed as the YZ and the XZ projections. The symmetry plane is shown in bright green. (b) False-colored optical image of the device. J_1 and J_2 indicates the two symmetric Josephson junctions (not visible on this scale). (c) A lumped-element circuit model of the device and its coupling to the environment through the strongly coupled port. Ideally, the qubit (quadrupolar) mode is linearly decoupled from the port.

$T_{1,m}^P = 0.34$ ms for the mediator mode by direct emission spectroscopy from the same port [23, 31, 32], and thus estimate $T_{1,q}^P = 2.6$ seconds for the qubit mode. To control the otherwise protected qubit mode, we add a weakly coupled port (W, shown in orange in Fig. 2(a)) that minimally perturbs the symmetry.

Readout of the qubit mode.—We perform a dispersive readout of the qubit mode in reflection. A SNAIL parametric amplifier (SPA) [33] is employed on the output line to provide 26 dB gain in the phase-sensitive mode. The readout resonator is driven from the strongly coupled port at frequency $\omega_d = \omega_r + \chi_{qr}/2$ to maximize the differential phase shift, where ω_r is the dressed resonator frequency when the dimon is in the ground state. The reflected wave is integrated for a time τ_{int} to obtain a demodulated quadrature signal $S(\tau_{\text{int}}) = \sqrt{\kappa_r} \int_0^{\tau_{\text{int}}} a_{\text{out}}(t) \mathcal{K}(t) dt$. $\mathcal{K}(t)$ is an experimentally obtained demodulation envelope [34], proportional to $|\langle a_{\text{out}}^g(t) - a_{\text{out}}^e(t) \rangle|$, where $a_{\text{out}}^{g,e}(t)$ is the instantaneous output wave amplitude corresponding to the qubit being in $|g\rangle$ (ground state) or $|e\rangle$ (excited state).

At each readout power, there is an optimum integration time beyond which the readout is no longer limited by discrimination error but by qubit decay and leakage during the readout. To determine the choice of readout time and power, we apply a two-step readout pulse [20], depicted in Fig. 3(a). Unlike a standard “box-car” (or “gated”) pulse, this technique ramps up the resonator faster than its natural ring-up time (κ_r^{-1}), improving the signal-to-noise ratio (SNR) at short duration ($\tau \sim \kappa_r^{-1}$) [30]. The assignment error of the binary readout outcome $\{0, 1\}$ (with respect to an optimum threshold) is calculated as $\varepsilon_R = [P(0|e) + P(1|g)]/2$, where

$P(x|\psi)$ is the probability that the measurement outcome is x given the qubit is prepared in $|\psi\rangle$. Note that, we use the labels $\{0, 1\}$ to distinguish the readout outcomes from the underlying states $|g\rangle$ and $|e\rangle$. In Fig. 3(a), we plot the assignment error, each evaluated from 100 000 shots, across varying integration times τ_{int} and steady-state photon number \bar{n}_r in the resonator. This plot instructs us on an optimal readout duration for each readout power.

Fast control of the readout resonator.—The integration time does not accurately represent the “readout duration” of practical interest. A relevant definition of readout duration measures the time during which the qubit is *unavailable for other operations*. Indeed, after the boxcar readout drive is turned off, the “tail” of the readout signal persists and *continues to dephase the qubit* for a timescale $\tau \sim 10/\kappa_r$, preventing any high fidelity qubit operations. This is shown by plotting the measurement rate, $\mathcal{M}(t) \propto |\langle \alpha_g(t) - \alpha_e(t) \rangle|^2$ (black) in Fig. 3(c). Therefore, the readout duration should be defined as the interval from the beginning of the readout pulse to the instant beyond which the photon-induced dephasing rate is inconsequential compared to the bare dephasing rate of the qubit.

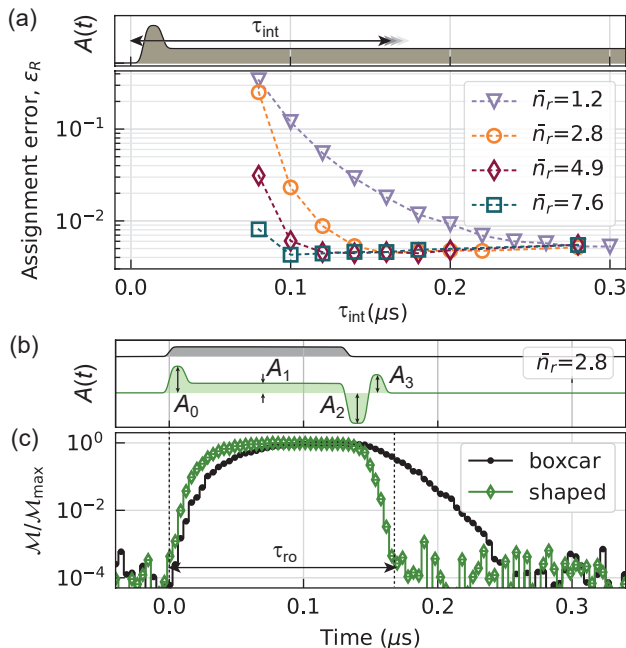


Figure 3. Readout calibration. (a) Two-step readout pulse with an initial high power segment and (below) the readout assignment error plotted against integration time τ_{int} for varying readout powers (represented by steady-state intra-resonator photon number \bar{n}_r). (b) Envelopes of boxcar and shaped readout pulses, calibrated for a readout with $\bar{n}_r = 2.8$. (c) Normalized qubit measurement rates as a function of time. The readout duration, τ_{ro} is defined as the interval when the readout resonator is populated.

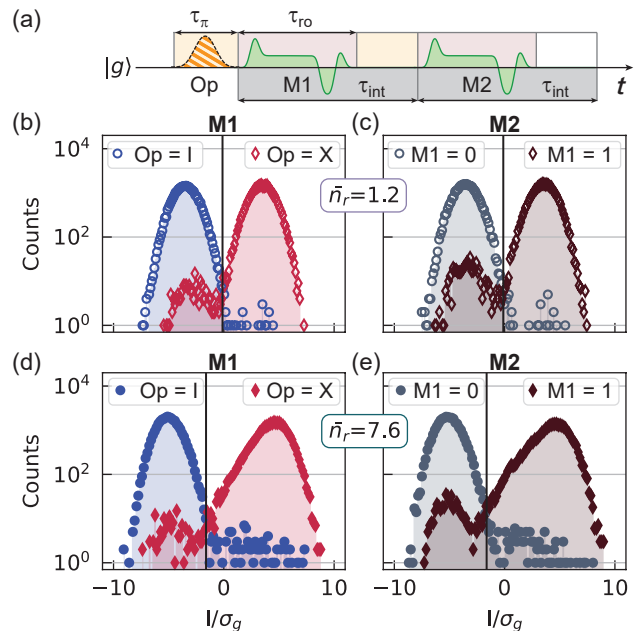


Figure 4. Single-shot readout performance. (a) Pulse sequence for the standard readout characterization. (b-e) Histograms of the integrated signal corresponding to the first (M1) and the second (M2) readout operations respectively for (b-c) $\bar{n}_r = 1.2$ and (d-e) $\bar{n}_r = 7.6$, constructed from 30 000 shots. The vertical lines represent the optimal demarcation thresholds in these settings. The readout-induced leakage at high-powers distorts the ‘e’-histogram from a Gaussian shape. This effect does not reflect in the readout outcome due to the choice of a *binary-threshold*, labeling them as the ‘e’-state.

We employ a pulse-shaping technique [19, 35] to minimize the readout duration for a given SNR at each readout power, using a four-step pulse, as shown in green in Fig. 3(b). The last two segments of this composite pulse empty the readout resonator unconditionally (regardless of the qubit state: $|g\rangle$ or $|e\rangle$), as illustrated by green markers in Fig. 3(c). The SPA in our experiment fails to respond as fast as the outgoing readout wave-packet, due to its limited 3 dB bandwidth of 8.3 MHz at the operating point, causing a slow-down of the wave-packet. Thus to capture the true resonator dynamics, the data in Fig. 3(c) is acquired with the SPA off (averaged over 100 000 shots). In a single-shot readout with the SPA on, we integrate for 140 ns longer than the duration of the readout pulse itself to completely acquire the wave-packet leaving the SPA. But this does not affect the readout duration defined above, as we confirm the restoration of qubit operations immediately after the readout pulse ends.

Single-shot readout performance.—We optimize the readout pulse across four different readout powers and characterize them using the standard procedure [23, 36]: We first initialize the qubit with pre-selection and prepare it in $|g\rangle$ or $|e\rangle$, and then apply two successive readout

pulses, as shown in Fig. 4(a). The binary readout fidelity $\mathcal{F} = [P(0|g) + P(1|e)]/2$ and the readout repeatability or *apparent* QND-ness $\mathcal{Q}_a = [\tilde{P}(0|0) + \tilde{P}(1|1)]/2$ are then calculated from the integrated readout histograms (See Fig. 4(b-e)), where $\tilde{P}(x|y)$ is the probability that the second readout outcome is x given the outcome for the first readout is y [21–23]. The readout duration, fidelity and repeatability for each of these readout settings are listed in Table I.

We emphasize that the correlation of two successive readout outcomes does not represent the *true* QND-ness in the presence of readout-induced leakage to higher states, if the readout fails to distinguish the leakage states from $|g\rangle$ and $|e\rangle$. This is suggested by the distortion of the ‘e’ histogram from a Gaussian shape in Fig. 4(d). The choice of the readout phase and binary threshold to maximally distinguish the $|g\rangle$ and $|e\rangle$ states will allocate the readout outcomes of the leakage states on one side of the threshold. Especially, if the parametric amplifier is operated in the phase sensitive mode to enhance the measurement efficiency, the information is contained in only one quadrature of the phase-space. This further prevents detection of leakage states when the readout is optimized for fidelity. As a result, the repeatability (Fig. 4(e)) will fail to report QND errors arising from readout-induced leakage. The true QND-ness \mathcal{Q} is related to the apparent QND-ness \mathcal{Q}_a by:

$$\mathcal{Q} = \mathcal{Q}_a - \frac{1}{2} [L_{(e)}P(1|\psi_l) + L_{(g)}P(0|\psi_l)]. \quad (1)$$

Here $L_{(g)}$ and $L_{(e)}$ are the leakage rates per readout from $|g\rangle$ and $|e\rangle$ respectively, and $P(x|\psi_l)$ is the probability of the measurement outcome to be x when the qubit transitions to leakage states. Typically, with a binary-thresholded readout $P(1|\psi_l) \sim 1$, and the repeatability metric significantly overestimates the QND-ness.

Pseudo-syndrome detection.—Detecting readout-induced leakage errors with binary-thresholded readout is especially challenging when the leakage rate is small compared to that of Pauli errors or discrimination errors. Yet even a small leakage rate could significantly degrade the performance of QEC. To address this limitation, we interleave repeated readout operations with randomized qubit flips, as depicted in Fig.5(a). Since any

BRO metric	$\bar{n}_r = 1.2$	$\bar{n}_r = 2.8$	$\bar{n}_r = 4.9$	$\bar{n}_r = 7.6$
RO Duration(ns)	240	160	120	100
Fidelity, \mathcal{F} (%)	99.63	99.63	99.61	99.54
Repeatability, \mathcal{Q}_a (%)	99.12	99.11	99.04	99.01
Leakage, L (%)	0.12	0.48	2.14	7.76
QND-ness, \mathcal{Q} (%)	99.00	98.63	96.90	91.25

Table I. Binary readout (BRO) metrics—Readout time, fidelity, repeatability and average leakage per readout along with the lower bound of QND-ness for readout pulses optimized for different powers.

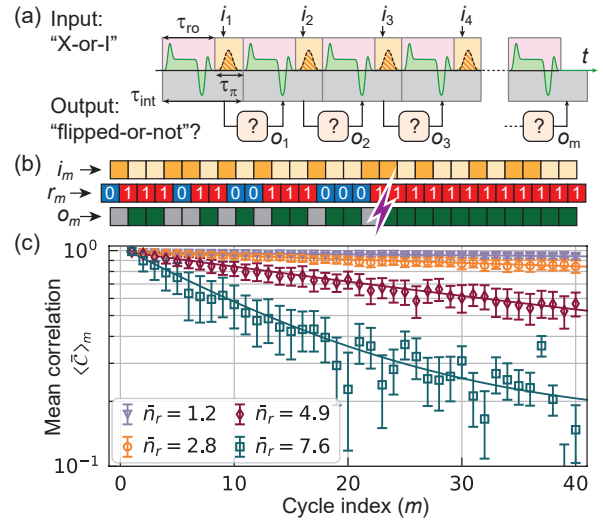


Figure 5. Readout performance under repeated applications. (a) Pulse sequence composed of interleaved readout operations and randomized bit-flip operations to benchmark the readout performance. (b) An example input “X-or-I” bit string i_m , ideal readout outcome bit-string r_m and the constructed output “flipped-or-not” bit-string o_m . The purple thunderbolt shows the occurrence of a leakage error corrupting all the subsequent outcomes. (c) Mean success probability $\langle \bar{C} \rangle_m$ of pseudo-syndrome detection as a function of detection cycle index m , for different \bar{n}_r . Solid curves correspond to exponential fits.

leakage event disrupts all subsequent operations on the qubit, the impact of a single leakage event is magnified with repetitions. This sequence mimics the syndrome detection in QEC as shown in Fig. 1, and thus the technique is named “pseudo-syndrome detection”. This technique provides a mean to characterize even small leakage errors and also contains the information about the readout fidelity and QND-ness. It is thus a *complete characterization* of the readout performance, requiring only binary-thresholded readout.

To characterize the readout operation, we perform the following steps. (1) Choose the sequence length M that indicates the total number of cycles in the pseudo-syndrome detection. (2) Construct K different randomizations for the input “X-or-I” bit-string $\{i_m\}$ and generate the corresponding interleaved sequences, as illustrated in Fig. 5(b). (3) From the outcomes r_m and r_{m-1} of successive readouts, obtain the output bit-string $\{o_m\}$ that detects “flipped-or-not”. (4) Compute the bit-wise correlation $C_m \in \{-1, +1\}$ for each experimental realization of the sequence (5) Perform N experimental realizations to compute the average bit-wise correlation \bar{C}_m for each random sequence. (6) Average over different randomizations to obtain the mean success probability $\langle \bar{C} \rangle_m$ for syndrome detection.

We perform pseudo-syndrome detection with four different readout pulses, each optimized for a given power.

We use a 100 ns pi-pulse which is slow compared to $1/|\delta_q|$ in order to prevent leakage from the bit-flip operation itself. The π -pulse is played during the padding time $\tau_{\text{pad}} = (\tau_{\text{int}} - \tau_{\text{ro}}) = 140$ ns between two readout pulses, while the previous readout wave-packet is still being acquired. We choose a sequence consisting of $M = 40$ readout operations with $K = 98$ different randomizations and evaluate $\langle \bar{\mathcal{C}} \rangle_m$ for each randomization. A Pauli error or a discrimination error locally corrupts one or two of the output bits, respectively. A leakage error, on the contrary, spoils the agreements for multiple rounds, as the qubit remains out of the computational subspace for several cycles. $\langle \bar{\mathcal{C}} \rangle_m$ decays exponentially with m due to the accumulation of leakage errors, as shown in Fig. 5(c). A higher power readout results in a faster decay of the success probability for syndrome detection. We fit the success probability to a decay model [37],

$$\langle \bar{\mathcal{C}} \rangle_m = \frac{1}{2} (A + B(1 - L)^m). \quad (2)$$

A and B contain the discrimination error, state initialization error and Pauli error during the sequence. $L = (L_{(g)} + L_{(e)})/2$ represents the average leakage probability per readout (see supplemental material [30] for details). We list L for each of the four optimized readout pulses in Table I. We estimate a lower bound on the QND-ness assuming that all the leakage errors arise from the $|e\rangle$ state and does not reflect in repeatability i.e., $P(1|\psi_i) = 1$. Our result highlights that optimizing a readout solely based on speed and fidelity may overlook significant leakage errors that harm the readout performance under repeated applications.

Conclusion.—We demonstrate a state-of-the art dispersive readout in terms of speed, fidelity and the QND-ness on a qubit intrinsically protected against Purcell decay. We issue a warning that the readout fidelity and apparent QND-ness may not be reliable metrics if the readout process induces significant leakage of the qubit state and we introduce a more faithful readout characterization technique. Future work involves a systematic investigation of the mechanisms for such readout-induced leakage [38]. Mitigating detrimental leakage at hardware level is a crucial step for further improvement of qubit readout.

The authors acknowledge A. Koottandavida, A. Miano, D. Weiss, J. Venkatraman, P. D. Parakh, R. Cortiñas, V. R. Joshi, W. Kalfus, and X. Xiao for illuminating discussions. This research was sponsored by the Army Research Office (ARO) under grant nos. W911NF-23-1-0051, by the Air Force Office of Scientific Research (AFOSR) under grant FA9550-19-1-0399 and by the U.S. Department of Energy (DoE), Office of Science, National Quantum Information Science Research Centers, Co-design Center for Quantum Advantage (C2QA) under contract number DE-SC0012704. The views and conclusions contained in this document are those of the au-

thors and should not be interpreted as representing the official policies, either expressed or implied, of the ARO, AFOSR, DoE or the US Government. The US Government is authorized to reproduce and distribute reprints for Government purposes notwithstanding any copyright notation herein. Fabrication facilities use was supported by the Yale Institute for Nanoscience and Quantum Engineering (YINQE) and the Yale SEAS Cleanroom. L.F. is a founder and shareholder of Quantum Circuits Inc. (QCI).

* sumeru.hazra@yale.edu, wei.dai.wd279@yale.edu; These two authors contributed equally

† michel.devoret@yale.edu

- [1] D. Ristè, J. G. van Leeuwen, H.-S. Ku, K. W. Lehnert, and L. DiCarlo, *Phys. Rev. Lett.* **109**, 050507 (2012).
- [2] C. Cabrillo, J. I. Cirac, P. García-Fernández, and P. Zoller, *Phys. Rev. A* **59**, 1025 (1999).
- [3] K. Lalumière, J. M. Gambetta, and A. Blais, *Phys. Rev. A* **81**, 040301 (2010).
- [4] D. Riste, M. Dukalski, C. Watson, G. De Lange, M. Tiggelman, Y. M. Blanter, K. W. Lehnert, R. Schouten, and L. DiCarlo, *Nature* **502**, 350 (2013).
- [5] N. Ofek, A. Petrenko, R. Heeres, P. Reinhold, Z. Leghtas, B. Vlastakis, Y. Liu, L. Frunzio, S. M. Girvin, L. Jiang, *et al.*, *Nature* **536**, 441 (2016).
- [6] L. Hu, Y. Ma, W. Cai, X. Mu, Y. Xu, W. Wang, Y. Wu, H. Wang, Y. Song, C.-L. Zou, *et al.*, *Nature Physics* **15**, 503 (2019).
- [7] V. Sivak, A. Eickbusch, B. Royer, S. Singh, I. Tsioutsios, S. Ganjam, A. Miano, B. Brock, A. Ding, L. Frunzio, *et al.*, *Nature* **616**, 50 (2023).
- [8] S. Krinner, N. Lacroix, A. Remm, A. Di Paolo, E. Genois, C. Leroux, C. Hellings, S. Lazar, F. Swiadek, J. Herrmann, *et al.*, *Nature* **605**, 669 (2022).
- [9] G. Q. AI, *Nature* **614**, 676 (2023).
- [10] Z. Ni, S. Li, X. Deng, Y. Cai, L. Zhang, W. Wang, Z.-B. Yang, H. Yu, F. Yan, S. Liu, *et al.*, *Nature* **616**, 56 (2023).
- [11] V. B. Braginsky and F. Y. Khalili, *Rev. Mod. Phys.* **68**, 1 (1996).
- [12] M. McEwen, D. Kafri, J. Chen, J. Atalaya, K. Satzinger, C. Quintana, P. V. Klimov, D. Sank, C. M. Gidney, A. Fowler, *et al.*, *Nature Communications* **12**, 1761 (2021).
- [13] A. Wallraff, D. I. Schuster, A. Blais, L. Frunzio, R.-S. Huang, J. Majer, S. Kumar, S. M. Girvin, and R. J. Schoelkopf, *Nature* **431**, 162 (2004), publisher: Nature Publishing Group.
- [14] A. Blais, A. L. Grimsmo, S. M. Girvin, and A. Wallraff, *Rev. Mod. Phys.* **93**, 025005 (2021).
- [15] D. Sank, Z. Chen, M. Khezri, J. Kelly, R. Barends, B. Campbell, Y. Chen, B. Chiaro, A. Dunsworth, A. Fowler, E. Jeffrey, E. Lucero, *et al.*, *Phys. Rev. Lett.* **117**, 190503 (2016).
- [16] R. Shillito, A. Petrescu, J. Cohen, J. Beall, M. Hauru, M. Ganahl, A. G. Lewis, G. Vidal, and A. Blais, *Phys. Rev. Appl.* **18**, 034031 (2022).
- [17] B. M. Varbanov, F. Battistel, B. M. Tarasinski, V. P.

- Ostroukh, T. E. O'Brien, L. DiCarlo, and B. M. Terhal, npj Quantum Information **6**, 102 (2020).
- [18] E. Jeffrey, D. Sank, J. Y. Mutus, T. C. White, J. Kelly, R. Barends, Y. Chen, Z. Chen, B. Chiaro, A. Dunsworth, *et al.*, Phys. Rev. Lett. **112**, 190504 (2014).
- [19] C. C. Bultink, M. A. Rol, T. E. O'Brien, X. Fu, B. C. S. Dikken, C. Dickel, R. F. L. Vermeulen, J. C. de Sterke, A. Bruno, R. N. Schouten, and L. DiCarlo, Phys. Rev. Appl. **6**, 034008 (2016).
- [20] T. Walter, P. Kurpiers, S. Gasparinetti, P. Magnard, A. Potočnik, Y. Salathé, M. Pechal, M. Mondal, M. Oppliger, C. Eichler, and A. Wallraff, Phys. Rev. Appl. **7**, 054020 (2017).
- [21] S. Touzard, A. Kou, N. E. Frattini, V. V. Sivak, S. Puri, A. Grimm, L. Frunzio, S. Shankar, and M. H. Devoret, Phys. Rev. Lett. **122**, 080502 (2019).
- [22] R. Dassonneville, T. Ramos, V. Milchakov, L. Planat, E. Dumur, F. Foroughi, J. Puertas, S. Leger, K. Bharadwaj, J. Delaforce, C. Naud, W. Hasch-Guichard, J. J. García-Ripoll, N. Roch, and O. Buisson, Phys. Rev. X **10**, 011045 (2020).
- [23] Y. Sunada, S. Kono, J. Ilves, S. Tamate, T. Sugiyama, Y. Tabuchi, and Y. Nakamura, Phys. Rev. Appl. **17**, 044016 (2022).
- [24] J. M. Gambetta, A. A. Houck, and A. Blais, Phys. Rev. Lett. **106**, 030502 (2011).
- [25] I. Diniz, E. Dumur, O. Buisson, and A. Auffèves, Phys. Rev. A **87**, 033837 (2013).
- [26] T. Roy, S. Kundu, M. Chand, S. Hazra, N. Nehra, R. Cosmic, A. Ranadive, M. P. Patankar, K. Damle, and R. Vijay, Phys. Rev. Appl. **7**, 054025 (2017).
- [27] F. Pfeiffer, M. Werninghaus, C. Schweizer, N. Bruckmoser, L. Koch, N. J. Glaser, G. Huber, D. Bunch, F. X. Haslbeck, M. Knudsen, *et al.*, arXiv preprint arXiv:2312.16988 (2023).
- [28] D. Pozar, *Microwave Engineering*, Addison-Wesley series in electrical and computer engineering (Addison-Wesley, 1990).
- [29] J. Gambetta, A. Blais, D. I. Schuster, A. Wallraff, L. Frunzio, J. Majer, M. H. Devoret, S. M. Girvin, and R. J. Schoelkopf, Phys. Rev. A **74**, 042318 (2006).
- [30] See Supplemental Material for additional information and data of the experiments.
- [31] M. Mirhosseini, E. Kim, X. Zhang, A. Sipahigil, P. B. Dieterle, A. J. Keller, A. Asenjo-Garcia, D. E. Chang, and O. Painter, Nature **569**, 692 (2019).
- [32] Y. Lu, A. Bengtsson, J. J. Burnett, E. Wiegand, B. Suri, P. Krantz, A. F. Roudsari, A. F. Kockum, S. Gasparinetti, G. Johansson, *et al.*, npj Quantum Information **7**, 35 (2021).
- [33] N. E. Frattini, V. V. Sivak, A. Lingenfelter, S. Shankar, and M. H. Devoret, Phys. Rev. Appl. **10**, 054020 (2018).
- [34] J. Gambetta, W. A. Braff, A. Wallraff, S. M. Girvin, and R. J. Schoelkopf, Phys. Rev. A **76**, 012325 (2007).
- [35] D. T. McClure, H. Paik, L. S. Bishop, M. Steffen, J. M. Chow, and J. M. Gambetta, Phys. Rev. Appl. **5**, 011001 (2016).
- [36] F. Swiadek, R. Shillito, P. Magnard, A. Remm, C. Hellings, N. Lacroix, Q. Ficheux, D. C. Zanuz, G. J. Norris, A. Blais, S. Krimmer, and A. Wallraff, "Enhancing dispersive readout of superconducting qubits through dynamic control of the dispersive shift: Experiment and theory," (2023), arXiv:2307.07765 [quant-ph].
- [37] C. J. Wood and J. M. Gambetta, Phys. Rev. A **97**, 032306 (2018).
- [38] M. F. Dumas, B. Groleau-Paré, A. McDonald, M. H. Muñoz-Arias, C. Lledó, B. D'Anjou, and A. Blais, arXiv preprint arXiv:2402.06615 (2024).

Supplemental Material for “Benchmarking the readout of a superconducting qubit for repeated measurements”

S. Hazra,^{1,*} W. Dai,^{1,*} T. Connolly,¹ P. D. Kurilovich,¹ Z. Wang,¹ L. Frunzio,¹ and M. H. Devoret^{1,†}

¹*Department of Applied Physics, Yale University, New Haven, Connecticut 06520, USA
and Yale Quantum Institute, Yale University, New Haven, Connecticut 06520, USA*

CONTENTS

I. Undriven Hamiltonian of the dimon coupled to a readout resonator	1
A. Dimon Hamiltonian and energy spectrum	1
B. Mediated dispersive interaction between qubit and resonator	2
II. Experimental device	3
A. Cryogenic set-up	3
B. Device parameters	4
C. Thermal population	4
III. Purcell protection	5
A. Purcell decay rate: Circuit model simulation	5
B. Measurement of Purcell decay rate	6
IV. Calibration of the readout pulse	7
A. Resonator non-linearity and photon number calibration	7
B. Readout pulse shaping	8
C. Delay caused by the SPA	8
V. Review of other dispersive readouts and Purcell filters	9
VI. Readout-induced state transitions	9
A. Readout-induced decay	9
B. Readout-induced leakage	10
VII. Pseudo-syndrome detection technique	11
A. Output bit-string processing	11
B. Leakage models	12
References	13

I. UNDRIVEN HAMILTONIAN OF THE DIMON COUPLED TO A READOUT RESONATOR

We derive the undriven Hamiltonian of the dimon-resonator system in this appendix. We first derive the dimon Hamiltonian alone (from a lumped-element circuit model), and then we include the readout resonator and find an analytical expression for the dispersive shift from the linearly uncoupled qubit mode.

A. Dimon Hamiltonian and energy spectrum

Here we derive the Hamiltonian of the dimon artificial molecule, which consists of two Josephson junctions and three capacitors, as schematized in the gray box in Fig. S1(b). This circuit was originally proposed as *Tunable Coupling Qubit* [1] with two SQUIDs instead of two Josephson junctions. We pick the node fluxes $\hat{\Phi}_1$ and $\hat{\Phi}_2$ defined from branch voltage across C_1 and C_2 (with the center node chosen as the ground) as the dynamical variables. The Lagrangian of the circuit can be written as:

$$\hat{\mathcal{L}} = \frac{1}{2} \left[C_1 \dot{\hat{\Phi}}_1^2 + C_2 \dot{\hat{\Phi}}_2^2 + C_s (\dot{\hat{\Phi}}_2 - \dot{\hat{\Phi}}_1)^2 \right] + E_{J1} \cos \left(\frac{\hat{\Phi}_1}{\phi_0} \right) + E_{J2} \cos \left(\frac{\hat{\Phi}_2}{\phi_0} \right) \quad (\text{S1})$$

with $\phi_0 = \hbar/(2e)$ being the reduced flux quantum. The Hamiltonian can be obtained by a Legendre transform on the Lagrangian:

$$\hat{\mathcal{H}} = \frac{s_{11}}{2} \hat{Q}_1^2 + \frac{s_{22}}{2} \hat{Q}_2^2 + s_{12} \hat{Q}_1 \hat{Q}_2 - E_{J1} \cos \left(\frac{\hat{\Phi}_1}{\phi_0} \right) - E_{J2} \cos \left(\frac{\hat{\Phi}_2}{\phi_0} \right) \quad (\text{S2})$$

where

$$s_{11} = \frac{C_s + C_2}{C_1 C_2 + C_s (C_1 + C_2)}$$

$$s_{22} = \frac{C_s + C_1}{C_1 C_2 + C_s (C_1 + C_2)}$$

$$s_{12} = \frac{C_s}{C_1 C_2 + C_s (C_1 + C_2)}$$

are elements of the inverse-capacitance (elastance) matrix. It is worth pointing out that the dimon circuit is equivalent to that of two capacitively coupled transmons, only with the shunting capacitance C_s between node 1 and 2 larger than the commonly achievable coupling capacitance between two transmons.

We include the effect of offset charge by considering external gate voltages $V_{g,1}$ ($V_{g,2}$) acting on node 1 (2) via $C_{g,1}$ ($C_{g,2}$), that introduces extra kinetic terms to the variational equation of motion:

$$\delta \int_{t_i}^{t_f} \left(\hat{\mathcal{L}} + \sum_{i=1,2} C_{g,i} V_{g,i} (\dot{\hat{\Phi}}_i - V_{g,i}) \right) dt = 0 \quad (\text{S3})$$

Thus they enter the Hamiltonian as displacements on the charge variables: $\hat{Q}_i \rightarrow \hat{Q}_i - Q_{g,i}$ ($i = 1, 2$), with $Q_{g,1} = C_{g,1}V_{g,1}$ and $Q_{g,2} = C_{g,2}V_{g,2}$ referred to as offset charges on the two nodes.

For the interest of this work, the circuit is designed to have the symmetry: $C_1 = C_2 = C_J$ and $E_{J1} = E_{J2} = E_J$. We further denote $\hat{\Phi}_q = (\hat{\Phi}_1 + \hat{\Phi}_2)/2$ for the *quadrupolar* degree of freedom and $\hat{\Phi}_m = (\hat{\Phi}_1 - \hat{\Phi}_2)/2$ for the *dipolar* degree of freedom as indicated in Fig. S1(a). Then the Hamiltonian can be reduced to:

$$\hat{\mathcal{H}}_D = \frac{e^2(\hat{n}_q - n_{g,q})^2}{C_J} + \frac{e^2(\hat{n}_m - n_{g,m})^2}{C_J + 2C_s} - 2E_J \cos \hat{\varphi}_q \cos \hat{\varphi}_m \quad (\text{S4})$$

where $\hat{\varphi}_k = \hat{\Phi}_k/\phi_0$ and $\hat{n}_k = \hat{Q}_k/2e$ ($k = q, m$) are canonical variables, $n_{g,q} = (Q_{g,1} + Q_{g,2})/2e$ and $n_{g,m} = (Q_{g,1} - Q_{g,2})/2e$ are the effective offset charges viewed by the qubit mode and mediator mode respectively.

The charging energies

$$E_{c,q} = \frac{e^2}{2(2C_J)}, \quad E_{c,m} = \frac{e^2}{2(2C_J + 4C_s)}$$

are designed to be small compared E_J , ensuring both qubit and mediator modes to be in the transmon regime[2]. As a result, the first few energy levels of dimon are expected to be insensitive to offset charges, which we'll neglect for the rest of this work. It is helpful to introduce creation and annihilation operators for the two modes ($k = q, m$):

$$\hat{\varphi}_k = \left(\frac{E_{c,k}}{E_J}\right)^{1/4} (\hat{a}_k^\dagger + \hat{a}_k), \quad (\text{S5})$$

$$\hat{n}_k = \frac{i}{2} \left(\frac{E_J}{E_{c,k}}\right)^{1/4} (\hat{a}_k^\dagger - \hat{a}_k) \quad (\text{S6})$$

We expand the product of two cosines up to 4th order and keep only the non-rotating terms:

$$\hat{\mathcal{H}}_{\text{nl}} = -2E_J \left(\cos \hat{\varphi}_q \cos \hat{\varphi}_m + \frac{\hat{\varphi}_q^2 + \hat{\varphi}_m^2}{2} \right) \quad (\text{S7})$$

$$\approx -\frac{E_{c,q}}{2} (\hat{a}_q^\dagger)^2 \hat{a}_q^2 - (E_{c,q} + \sqrt{E_{c,q}E_{c,m}}) \hat{a}_q^\dagger \hat{a}_q \quad (\text{S8})$$

$$- \frac{E_{c,m}}{2} (\hat{a}_m^\dagger)^2 \hat{a}_m^2 - (E_{c,m} + \sqrt{E_{c,q}E_{c,m}}) \hat{a}_m^\dagger \hat{a}_m \\ - 2\sqrt{E_{c,q}E_{c,m}} \hat{a}_q^\dagger \hat{a}_q \hat{a}_m^\dagger \hat{a}_m$$

that show up as the Kerr nonlinearity and Lamb shift for the qubit and mediator mode, and a cross-Kerr interaction between the two modes.

The Hamiltonian in Eq. S4 can thus be rewritten into:

$$\hat{\mathcal{H}}_D = \hbar\omega_q \hat{a}_q^\dagger \hat{a}_q - \frac{E_{c,q}}{2} (\hat{a}_q^\dagger)^2 \hat{a}_q^2 + \hbar\omega_m \hat{a}_m^\dagger \hat{a}_m \\ - \frac{E_{c,m}}{2} (\hat{a}_m^\dagger)^2 \hat{a}_m^2 + \hbar\chi_{qm} \hat{a}_q^\dagger \hat{a}_q \hat{a}_m^\dagger \hat{a}_m \quad (\text{S9})$$

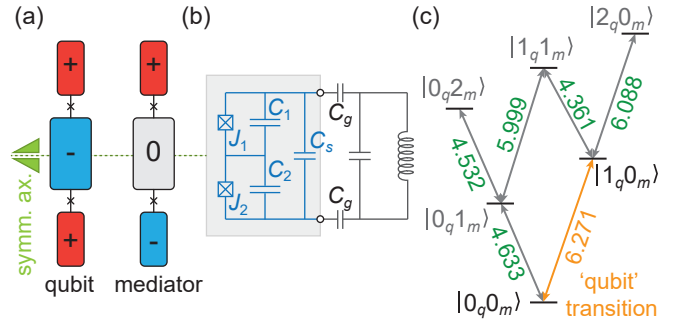


Figure S1. Symmetry in dimon. (a) The two normal modes of a symmetric dimon, termed as the ‘qubit’ and the ‘mediator’ mode. (b) The lumped element circuit model of dimon. (c) The energy level diagram of dimon in the low energy subspace. The transition frequencies in GHz unit are shown in green. The $|0_q0_m\rangle$ to $|1_q0_m\rangle$ transition is used as the qubit (shown in orange in the diagram).

where $\hbar\omega_q = 4\sqrt{E_{c,q}E_J} - E_{c,q} - \sqrt{E_{c,q}E_{c,m}}$ is the energy difference between $|1_q0_m\rangle$ and $|0_q0_m\rangle$, $\hbar\omega_m = 4\sqrt{E_{c,m}E_J} - E_{c,m} - \sqrt{E_{c,q}E_{c,m}}$ is the energy difference between $|0_q1_m\rangle$ and $|0_q0_m\rangle$, and $\hbar\chi_{qm} = -2\sqrt{E_{c,q}E_{c,m}}$ is the full cross-Kerr shift between the qubit mode and mediator mode.

B. Mediated dispersive interaction between qubit and resonator

As illustrated in Fig. S1(b), the symmetry of the dimon circuit along with the coupling capacitances C_g guarantees that the readout resonator is capacitively coupled to only the mediator (dipolar) mode, but not to the qubit (quadrupolar) mode. Using the creation and annihilation operators, the full circuit Hamiltonian can be expressed as:

$$\hat{\mathcal{H}} = \hat{\mathcal{H}}_D + \omega_r \hat{a}_r^\dagger \hat{a}_r - g_{mr} (\hat{a}_m^\dagger - \hat{a}_m) (\hat{a}_r^\dagger - \hat{a}_r) \quad (\text{S10})$$

$$\approx \sum_{k=q,m,r} \omega_k \hat{a}_k^\dagger \hat{a}_k + g_{mr} (\hat{a}_m^\dagger \hat{a}_r + \hat{a}_m \hat{a}_r^\dagger) + \hat{\mathcal{H}}_{\text{nl}} \quad (\text{S11})$$

In the second line we have applied the rotating-wave approximation (RWA).

We further diagonalize the linear part of the Hamiltonian by a unitary transformation $\hat{U} = \exp\{\Lambda(\hat{a}_r^\dagger \hat{a}_m - \hat{a}_r \hat{a}_m^\dagger)\}$:

$$\hat{U}^\dagger \hat{\mathcal{H}} \hat{U} = \omega_q \hat{a}_q^\dagger \hat{a}_q + \tilde{\omega}_m \hat{a}_m^\dagger \hat{a}_m + \tilde{\omega}_r \hat{a}_r^\dagger \hat{a}_r + \hat{U}^\dagger \hat{\mathcal{H}}_{\text{nl}} \hat{U} \quad (\text{S12})$$

with $\Lambda = (1/2) \arctan(2g_{mr}/\Delta_{mr})$, where we have denoted the detuning between mediator and resonator as $\Delta_{mr} = \omega_m - \omega_r$. The dressed mode frequencies after the

transformation are given by:

$$\begin{aligned}\tilde{\omega}_m &= \frac{1}{2} \left(\omega_m + \omega_r - \sqrt{\Delta_{mr}^2 + 4g_{mr}^2} \right) \approx \omega_m + \frac{g_{mr}^2}{\Delta_{mr}} \\ \tilde{\omega}_r &= \frac{1}{2} \left(\omega_m + \omega_r + \sqrt{\Delta_{mr}^2 + 4g_{mr}^2} \right) \approx \omega_r - \frac{g_{mr}^2}{\Delta_{mr}}\end{aligned}$$

Regarding $\hat{U}^\dagger \mathcal{H}_{\text{nl}} \hat{U}$ we make the following observations: The first line of Eq.S8 remains identical under the transformation. The second line of Eq.S8 is the same as a transmon Hamiltonian, and therefore results in a dispersive shift to the resonator (of $|0_q 1_m$ versus $|0_q 0_m$ states):

$$\chi_{mr} = -2 \frac{g_{mr}^2 E_{c,m} / \hbar}{\Delta_{mr} (\Delta_{mr} - E_{c,m} / \hbar)} \quad (\text{S13})$$

We then want to expand the third line of Eq.S8 up to 2nd power of g_{mr} / Δ_{mr} :

$$\begin{aligned}\hat{U}^\dagger (\hbar \chi_{qm} \hat{a}_q^\dagger \hat{a}_q \hat{a}_m^\dagger \hat{a}_m) \hat{U} &= \hbar \chi_{qm} \hat{a}_q^\dagger \hat{a}_q \left(\hat{a}_m^\dagger \hat{a}_m + \frac{g_{mr}^2}{\Delta_{mr}^2} \hat{a}_r^\dagger \hat{a}_r \right. \\ &\quad \left. - \frac{g_{mr}}{\Delta_{mr}} (\hat{a}_m^\dagger \hat{a}_r + \hat{a}_m \hat{a}_r^\dagger) \right)\end{aligned}$$

Note that the 2nd order perturbation from the last term gives rise to a correction to $\hat{a}_q^\dagger \hat{a}_q \hat{a}_r^\dagger \hat{a}_r$ that is 2nd order in g_{mr} / Δ_{mr} . Accounting for that, the dispersive shift to the resonator (of $|1_q 0_m$ versus $|0_q 0_m$ states) has the form:

$$\chi_{qr} = \frac{g_{mr}^2 \chi_{qm}}{\Delta_{mr}^2} - \frac{(g_{mr} \chi_{qm})^2}{\Delta_{mr} + \chi_{qm}} = \frac{g_{mr}^2 \chi_{qm}}{\Delta_{mr} (\Delta_{mr} + \chi_{qm})} \quad (\text{S14})$$

It is worth emphasizing that the *mediated* dispersive interaction between the qubit and resonator does not depend on the qubit-resonator detuning.

II. EXPERIMENTAL DEVICE

A. Cryogenic set-up

The device is fabrication on Heat Exchanger Method (HEM) sapphire with thin film aluminum capacitor pads and Al-AlO_x-Al junctions formed by bridge-free technique. Both the readout cavity and the waveguide is made of 6061 Aluminum alloy. Our experiments are conducted in an Oxford TritonTM dilution refrigerator with a base temperature reaching $T_{\text{MXC}} = 28$ mK. A schematic of the cryogenic experimental set-up is shown in Fig. S2. The 3D cavity along with the waveguide coupler is placed inside a hollow copper cylinder lined with carbon black and sealed inside a light-tight Cryoperm magnetic shield. The copper cylinder thermalizes with the mixing chamber of the dilution fridge. To protect

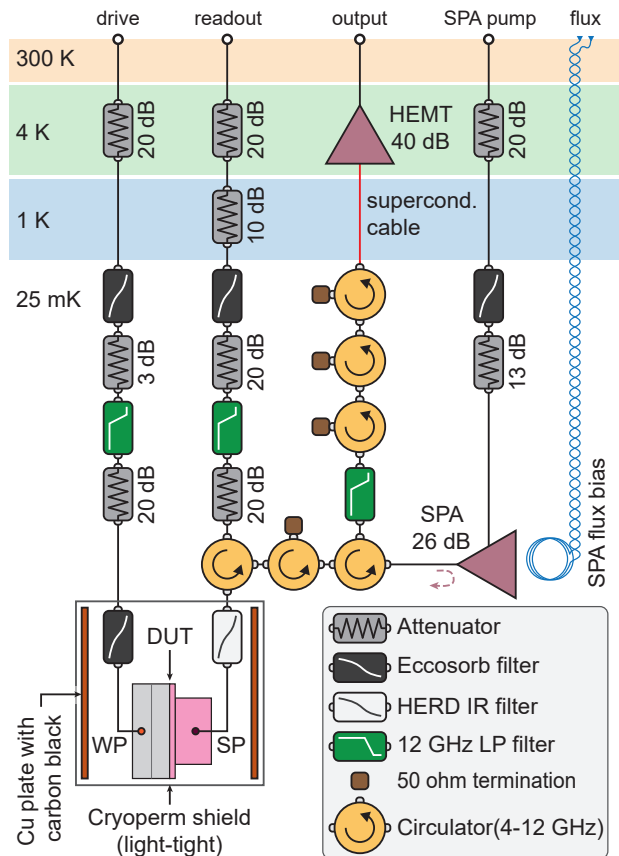


Figure S2. Cryogenic experimental setup at different stages of the dilution fridge.

the device from infrared radiation from the transmission lines, we employ an Eccosorb filter at the weakly coupled port and a high-energy radiation drain (HERD)[3] filter at the strongly coupled port. The HERD filter has negligible losses at readout frequency, and therefore causes minimal efficiency degradation to the output line. Additionally, we use a low insertion loss triple-junction cryogenic circulator array ($S_{21} \sim 0.5$ dB total) to further minimize losses before the SPA. We operate the SPA in the phase-sensitive mode and calibrate it to produce 26 dB gain to suppress the added noise after the SPA.

The measurement efficiency η of the output chain is measured using the expression for the steady state SNR of the integrated signal.

$$\text{SNR}_{\text{SS}} = \eta \bar{n}_r \kappa_{\text{ext}} \tau_{\text{int}} \frac{8\chi_{qr}^2}{\chi_{qr}^2 + \kappa_r^2} \quad (\text{S15})$$

The external coupling rate κ_{ext} is power independent and is calculated from a circle fit on the quadrature signal from a low power reflection measurement. The total readout resonator line-width $\kappa_r = \kappa_{\text{ext}} + \kappa_{\text{int}}$ and the intra-resonator photon number are simultaneously measured from an independent experiment explained in Sec. IV A. κ_{int} is the effective internal loss rates of the readout res-

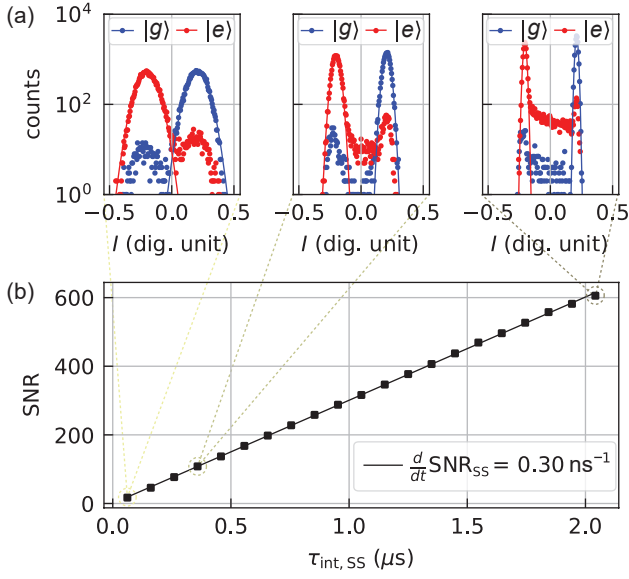


Figure S3. Steady state SNR vs time with $\bar{n}_r = 2.8$. (a) Integrated quadrature histograms consisting of 19 000 shots, projected on the I quadrature. Three such sets obtained with different integration times are shown. A Gaussian fit is used on each of them to extract the discriminability and SNR of the signal. (b) Plotted readout SNR as a function of integration time and a linear fit to extract the readout efficiency.

onator. The readout resonator dispersive shift χ_{qr} is calculated from the resonator response (phase-roll) when the qubit is prepared in $|g\rangle$ and $|e\rangle$ states. $\text{SNR}_{\text{SS}}(\tau_{\text{int}})$ is measured from the integrated quadrature histograms in the steady state for different integration times (τ_{int}). We use a linear fit to extract a slope:

$$\frac{d\text{SNR}_{\text{SS}}}{d\tau_{\text{int}}} = \eta \bar{n}_r \kappa_{\text{ext}} \frac{8\chi_{qr}^2}{\chi_{qr}^2 + \kappa_r^2} = 0.30 \text{ ns}^{-1} \quad (\text{S16})$$

The readout efficiency of the output chain (with 26 dB gain from SPA) is measured to be $\eta = 0.79 \pm 0.18$ from this relation, with the uncertainty dominantly arising from the fitting uncertainty of $\kappa_{\text{ext}}/2\pi = 11.6 \pm 1.4$ MHz.

B. Device parameters

We characterize the eigen-energies of the composite Hilbert space of the mediator and the qubit mode with total excitation, $(n_q + n_m) \leq 2$. We measure the transition frequencies between levels by climbing the two-dimensional ladder of the dimon molecule. See Fig. S1(c). The relevant frequencies, anharmonicities and the total resonator dispersive shift for the two modes of dimon are listed in Table. S1 along with the measured coherence on the two modes of the dimon molecule. The cross-Kerr interaction between the qubit and the mediator mode is measured to be $\chi_{qm}/2\pi = -272$ MHz. The readout res-

Entity	Qubit	Mediator
Frequency ($\omega/2\pi$) (GHz)	6.271	4.633
Anharmonicity ($\delta/2\pi$) (GHz)	-0.183	-0.101
Dispersive interaction ($\chi/2\pi$) (MHz)	-6.4	-8.5*
Relaxation time (T_1) (μs)	50.	71
Ramsey time (T_2^R) (μs)	36	18
Hahn echo time (T_2^E) (μs)	42	61

Table S1. Device parameters and coherence of the two modes of dimon. *Mediator mode dispersive shift is measured in a different cool-down with identical set up.

onator has a dressed frequency $\omega_r/2\pi = 7.515$ GHz when the dimon is in the ground state.

C. Thermal population

We perform a CW measurement using a vector network analyzer (VNA) to measure the thermal population in the first excited state of the qubit mode, $|1_q 0_m\rangle$ and the mediator mode, $|0_q 1_m\rangle$ of the dimon molecule. We measure a population of 0.26% and 1.30% respectively for the $|1_q 0_m\rangle$, and, $|0_q 1_m\rangle$ states from the phase space histograms (plotted in Fig. S4).

Assuming the system is in thermal equilibrium, we estimate an effective temperature of the device by computing the thermal population in the higher excited states of the molecule using the expression[4]:

$$P_{|i\rangle} = \frac{\exp(-E_i/k_B T)}{\sum_i \exp(-E_i/k_B T)} \quad (\text{S17})$$

We consider the first four levels $|0_q 0_m\rangle$, $|0_q 1_m\rangle$, $|1_q 0_m\rangle$, and, $|0_q 2_m\rangle$, beyond which the thermal population should be negligible. The measured higher state populations are consistent with a temperature $T = 51$ mK for

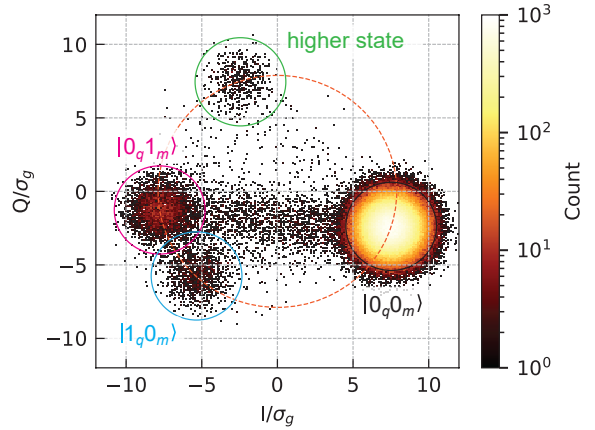


Figure S4. Thermal population of dimon measured through continuous wave reflection spectroscopy of the readout resonator using a VNA.

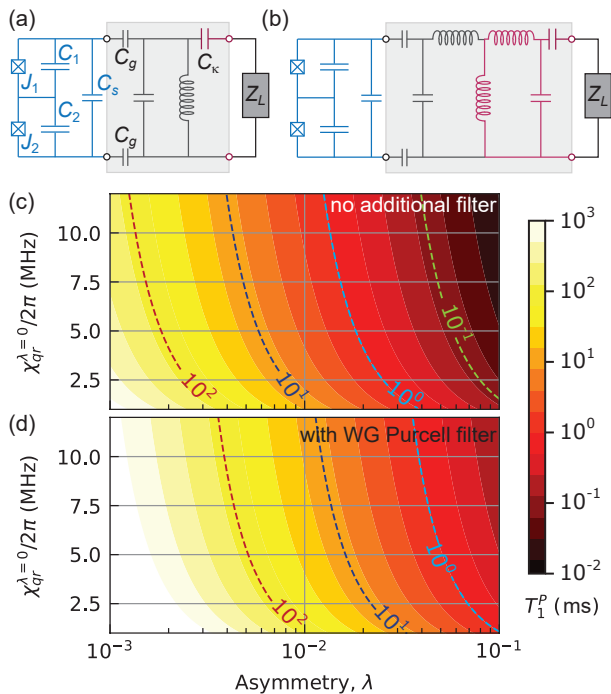


Figure S5. Purcell T_1 as a function of junction asymmetry (x-axis) and effective dispersive shift (y-axis). The dissipation seen by the qubit mode is computed using a lumped element circuit simulations with the transmission line modelled as a dissipative load. The weakly coupled port in the experimental device is neglected in this computation.

our device. This measurement also highlights the need for a *pre-selection readout* in our experiments, bringing down the thermal population well below 0.01%.

III. PURCELL PROTECTION

In this appendix, we explain the effect of junction asymmetry on the Purcell decay rate of the qubit from numerical analysis of two lumped-element circuits (with and without an external waveguide Purcell filter). Next, we describe the experimental technique to measure the Purcell decay rate of the qubit mode of the dimon into the strongly coupled port and the weakly coupled port respectively.

A. Purcell decay rate: Circuit model simulation

The intrinsic Purcell protection of the qubit mode in dimon relies on the geometric symmetry of the device. Typically, the uncertainty in junction fabrication is the main source of asymmetry for our device. We investigate the effect of junction asymmetry, defined as $\lambda = (E_{J1} - E_{J2}) / (E_{J1} + E_{J2})$, on the Purcell decay rate of the qubit mode.

First, we consider a dimon coupled to a resonator that is directly emitting into a transmission line, as shown in Fig. S5(a). We replace the transmission line with a $Z_L = 50\Omega$ load coupled to the resonator with a capacitor C_κ that sets the external coupling rate of the resonator to $\kappa_r/2\pi = 12$ MHz. First we construct the circuit with $\lambda = 0$ and choose $E_{J1} = E_{J2}$, $C_1 = C_2$ such that the qubit mode frequency and anharmonicity are $\omega_q/2\pi = 6.28$ GHz and $\delta_q/2\pi = -0.188$ GHz respectively, motivated by the target values of the experimental device. The dressed readout resonator frequency is kept fixed at $\omega_r/2\pi = 7.5$ GHz. The coupling capacitance C_g and the shunting capacitance C_s are varied to control the mediated qubit-resonator dispersive shift χ_{qr} , while keeping the dressed mediator mode frequency nominally unchanged at $\omega_m/2\pi \sim 4.58$ GHz. Next, we introduce a variable asymmetry in the junction ranging from $\lambda = 10^{-3}$ to 10^{-1} . As the asymmetry increases, the qubit mode inherits a dipole moment and subsequently inherits the losses from the resonator. In Fig. S5(c) we plot the Purcell decay time, T_1^P of the qubit mode as a function of the dispersive shift calculated at zero asymmetry, $\chi_{qr}^{\lambda=0}$ and the asymmetry parameter. We observe that even with a few percent of junction asymmetry, T_1^P exceeds few hundred microseconds even for $\chi_{qr}/2\pi = \kappa_r/2\pi = 12$ MHz.

Then, to model the aperture coupled waveguide coupler in our setup we include another filter mode in the circuit model, inductively coupled to the readout resonator (see Fig. S5(b)). We set the dressed frequency and external coupling of the filter mode to the experimentally measured values, $\omega_{PF}/2\pi = 8.08$ GHz and $\kappa_{PF}/2\pi = 0.153$ GHz, and set the shared inductance value such that the effective external coupling of the readout resonator is $\kappa_r/2\pi = 12$ MHz. We perform the same numerical simulation of varying the junction asymmetry and plot T_1^P in Fig. S5(d). As expected, the additional filter mode provides extra protection against Purcell decay even when there is some residual asymmetry. A few percent of junction asymmetry now results in $T_1^P > 1$ ms for $\chi_{qr}/2\pi = \kappa_r/2\pi = 12$ MHz.

Finally, to contrast the intrinsic Purcell protection of dimon (with 1% junction asymmetry) against an ordinary transmon, we simulate both the circuits, including the waveguide filter mode. We consider identical resonator and the waveguide filter mode parameters. The anharmonicities of the transmon and the qubit mode of the dimon are chosen to be identical $\delta_q/2\pi = -0.188$ GHz. The coupling capacitors are chosen such that at $\omega_q/2\pi = 6.28$ GHz, the resonator dispersive shifts of the transmon and the dimon are identical, $\chi_{qr}/2\pi = 6.16$ MHz. We scale the junction inductances with a varying factor to tune the qubit mode of dimon (or the transmon) and compute T_1^P and the dispersive shift χ_{qr} as a function of frequency, as shown in Fig. S6. The qubit mode embedded in dimon benefits from three order of

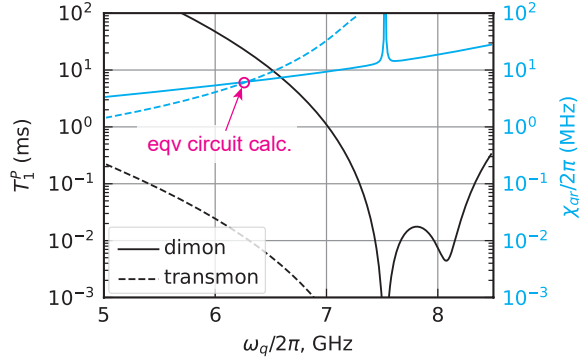


Figure S6. Comparing the the Purcell T_1 of a dimon (solid curve) with $\lambda = 1\%$ junction asymmetry with that of an equivalent transmon (dashed curve) using a lumped element circuit model. The second dip in T_1^P is due to the waveguide filter mode.

magnitude added protection compared to the transmon for a reasonable choice of asymmetry $\lambda = 1\%$. Note that, changing the junction inductance causes the mediator mode frequency to move, which results in a slow variation of the mediated dispersive shift χ_{qr} in dimon (solid blue curve) compared to a more dramatic change in the case of transmon (dashed blue curve). In dimon, the divergence of χ_{qr} when $\omega_q = \omega_r$ is due to the asymmetry and resulting linear hybridization between the qubit mode and the resonator.

B. Measurement of Purcell decay rate

Since the Purcell decay rate of the qubit mode is expected to be very small, it is difficult to directly measure it in experiments. Hence, we take a two step approach to estimate T_1^P of the qubit mode. We first measure the Purcell decay rate of the mediator mode which directly couples to the TE101 mode of the readout cavity and can spontaneously radiate into the strongly coupled port. We employ a direct emission spectroscopy technique[5–7] to measure the Purcell decay rate of the mediator mode. We apply a weak saturation tone on the mediator mode at its resonant frequency and fit the reflected quadrature signal to the expression (See Fig. S7(a)):

$$S_{11}(\omega_d) = 1 - \frac{\tilde{\Gamma}_1^P}{\Gamma_2} \frac{1 - i(\omega_m - \omega_d)/\Gamma_2}{1 + s + (\omega_m - \omega_d)^2/\Gamma_2^2} \quad (\text{S18})$$

where, s is a fit parameter representing the saturation of the mode under the CW drive,

$$s = \frac{\Omega^2}{(\Gamma_\uparrow + \Gamma_\downarrow)\Gamma_2} \quad (\text{S19})$$

and, finally,

$$T_1^P = \frac{1 - r_{\text{th}}}{1 + r_{\text{th}}} \frac{1}{\tilde{\Gamma}_1^P}, \quad (\text{S20})$$

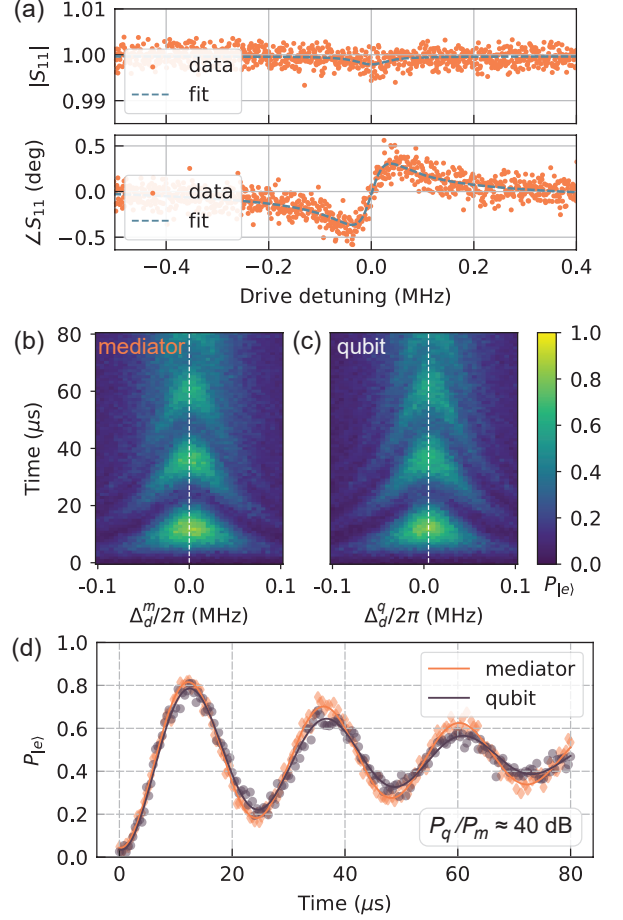


Figure S7. (a) The reflection spectrum of the mediator mode from direct continuous wave scattering and its fit to a model for complex reflection coefficient with a saturable mode. (b-c) Rabi oscillations on the two modes of dimon as a function of drive detuning. (d) Near identical Rabi rates, $\Omega_m/2\pi = 41.7$ kHz and $\Omega_q/2\pi = 41.2$ kHz obtained by driving with a power ratio $P'_q/P'_m \sim 43$ dB measured at the room temperature. Taking into account of the variation of input attenuation of the cryogenic setup at the two different frequencies, this translates to 40 dB power difference at the strongly couple port of the resonator.

where, $r_{\text{th}} \equiv P_{0_q1_m}/P_{0_q0_m}$ is the thermal excitation ratio measured independently (and reported in Sec. II C). From the fit, we find a Purcell decay time for the mediator mode, $T_{1,m}^P = 0.34$ ms.

To compute the Purcell decay rate of the qubit mode we compare the Rabi oscillation rates of the mediator and the qubit mode, when driven from the strongly coupled port. The Rabi Rate Ω of a mode for a certain drive power P applied on a given port is directly related to the radiation decay of that mode through that port:

$$\Gamma_1^P(\omega_d) = \frac{\Omega^2 \hbar \omega_d}{4P} \quad (\text{S21})$$

We measure a power ratio of $P'_q/P'_m \approx 43$ dB, at the

input of the dilution fridge (300 K), to achieve near identical Rabi rates of $\Omega_m/2\pi = 41.7$ kHz and $\Omega_q/2\pi = 41.2$ kHz on the mediator and qubit mode respectively. From an independent calibration of input line attenuation, this translates to a power ratio of $P_q/P_m \approx 40$ dB at the strongly-coupled port of the resonator. We use this calibration to estimate a Purcell $T_{1,q}^P = 2.6$ seconds for the qubit mode. Note that the measured Purcell T_1 in experiments exceeds the value predicted from the lumped circuit simulation by two orders of magnitude. This can be attributed to the multi-mode effect of the 3D cavities [8]. In our simulation we only kept two lowest frequency modes of the distributed 3D architecture containing the readout cavity and the waveguide Purcell filter.

Finally, to compute the Purcell decay rate through the weakly coupled port, we compare the Rabi rate on the qubit mode through the strong port and the weak port. Using S21 and the calibration of input attenuation of the drive line and the readout line, the Purcell decay rate through the weakly coupled port is estimated to be 0.4 seconds.

IV. CALIBRATION OF THE READOUT PULSE

The optimization of the readout pulse involves the photon number calibration, finding the optimum readout frequency and finally tuning the amplitudes of the piecewise constant pulse that expedites the evacuation of the readout resonator at the end of the readout. We also show that the self-Kerr of the readout resonator is non-negligible and needs to be included in the equation of motion to find the optimal pulse shape.

A. Resonator non-linearity and photon number calibration

In our device, to achieve a large dispersive shift, we strongly hybridize the mediator mode with the readout resonator. This causes the readout resonator to inherit some non-linearity from the participation of the Josephson junctions in the readout mode. Although, during readout we use a relatively small photon number compared to the critical photon number to bifurcate the readout resonator ($\bar{n}_r \ll -\kappa_r/3\sqrt{3}K$), the self-Kerr shift of the readout frequency is non-negligible. This has a rather small effect on the SNR, but crucially modifies the choice of drive detuning in readout pulse shaping. Furthermore, owing to the inherited self-Kerr, the *average photon number* in the readout resonator exhibits a non-linear reliance on the input drive power, necessitating a careful calibration of the average photon number.

To simultaneously calibrate the average photon-number and measure the Kerr non-linearity of the readout resonator, we assume a Duffing oscillator model for

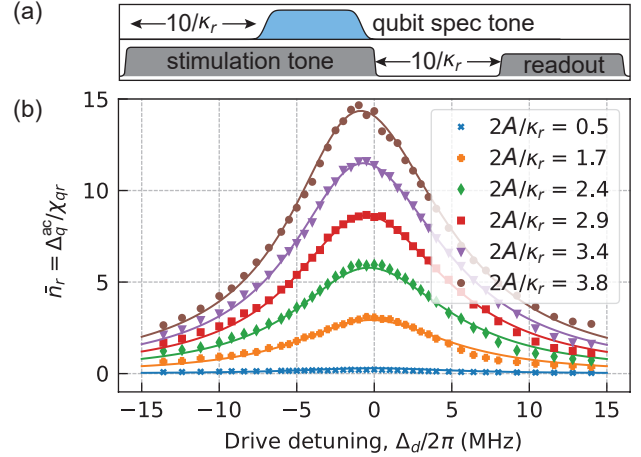


Figure S8. Measurement of the acquired non-linearity of the readout resonator. (a) The pulse sequence to measure average photon number in the readout resonator \bar{n}_r , as a function of the detuning and the amplitude of the applied readout tone. (b) The estimated intra-resonator photon number, measured from the ac Stark shift on the qubit is fitted to the Kerr oscillator model. From this fit, we simultaneously estimate the Kerr non-linearity, resonator line-width and the input line attenuation.

the readout resonator[9], where the leading non-linear term is given by K .

$$\dot{\alpha}(t) = - \left(i\Delta_d + iK|\alpha(t)|^2 + \frac{\kappa_r}{2} \right) \alpha(t) + A(t), \quad (\text{S22})$$

where Δ_d is the detuning of the drive from the resonance (measured at low power limit), $\alpha(t)$ is the instantaneous displacement of the oscillator in the phase space and $A(t) = \sqrt{\kappa_r} \bar{a}_{in}(t)$, where $\bar{a}_{in}(t)$ is the instantaneous amplitude of the input photon field. Since we do not have an accurate measure of drive amplitude at the readout port, we assume a complex scaling factor k_{sca} (to be determined from the fit) such that, $A(t) = k_{\text{sca}} a_{\text{DAC}}(t)$. We also assume that k_{sca} is frequency independent for the range of drive detuning Δ_d used in the experiment.

The classical steady-state response of such a Kerr oscillator, to the leading order of non-linearity is given by[9, 10]:

$$\left(i\Delta_d + iK|\alpha_{\text{ss}}|^2 + \frac{\kappa_r}{2} \right) \alpha_{\text{ss}} = A \quad (\text{S23})$$

The steady-state amplitude of the oscillator can be expressed in terms of the intra-resonator photon number, $|\alpha_{\text{ss}}|^2 = \bar{n}_r$. The latter can be quantified in terms of the ac Stark shift on the qubit and the qubit-resonator dispersive shift χ_{qr} . Experimentally, we perform a qubit spectroscopy under a resonator stimulation tone with varying Δ_d and $a_{\text{DAC}} = A/k_{\text{sca}}$ to record the ac Stark shift. The resonator stimulation tone is turned on $10/\kappa_r$ prior to the low power qubit probe tone around the qubit frequency, making sure the resonator has reached the

steady-state. We then turn off the stimulation tone and let the resonator ring-down for a duration $10/\kappa_r$, followed by a qubit readout. In Fig. S8(b) we plot the intra-resonator photon number (at steady-state) inferred from the ac Stark shift as a function of drive detuning Δ_d for different DAC amplitudes a_{DAC} . We fit the dependence with the Kerr-oscillator response given by Eq. S23 with three free parameters, K , κ_r and, $|k_{\text{sca}}|$, ($\{\kappa_r, K\} \in \mathbb{R}, k_{\text{sca}} \in \mathbb{C}$) which we determine from the fit.

$$\left[(\Delta_d + K\bar{n}_r)^2 + \frac{\kappa_r^2}{4} \right] \bar{n}_r = |k_{\text{sca}}|^2 |a_{\text{DAC}}|^2 \quad (\text{S24})$$

We have absorbed the phase of the displacement α on the LHS of the equation in the complex scaling factor k_{sca} . We obtain $\kappa_r/2\pi = 12$ MHz, $|k_{\text{sca}}| = 162$, and $K/2\pi = -60$ kHz. Note that the estimated κ_r from this experiment differs by about 3.4% from the one extracted from the direct reflection measurement of the resonator performed with a small steady state photon number, $\bar{n}_r \sim 2.8$. This is due to parametric excitation of the dimon to leakage states at higher probe power, causing an increase of effective line-width of the resonator.

B. Readout pulse shaping

To speed up the readout resonator ramp-up and ramp-down, we calibrate a four-stage readout pulse as described in the main text. Our goal is to maximally separate the two resonator trajectories $\alpha_g(t)$ and $\alpha_e(t)$ corresponding to the $|g\rangle$ and $|e\rangle$ states of the qubit respectively, under the constraint of maximum photon number and reset the resonator at the end of the pulse. Each section of the resonator control pulse intends to drive the resonator from one steady state to another. The initial high-amplitude response rapidly drives the resonator towards a large displaced state. But as soon as we reach the desired maximum photon number (\bar{n}_{max}) for the readout, we release the resonator to a smaller drive amplitude, letting it evolve towards the new steady state, maintaining the photon number below \bar{n}_{max} . The third stage speeds up the resonator once again, but this time in the opposite direction till we find a suitable point in phase space for a sharp ‘‘U-turn’’ and converge at the origin with the help of another high-amplitude segment. The third and fourth segment of the pulse causes a rapid driven ramp-down.

To find the exact shape of the four-stage pulse, we constrain the maximum photon number \bar{n}_{max} during the evolution and the total pulse duration. We vary the relative length and the amplitude of each section along with the pulse detuning to minimize the ratio of undesired measurement after the pulse ends to the desired measurement during the pulse. The measurement is quantified in terms of the integrated SNR over a period. Putting in a compact form, the shaped pulse corresponds to the

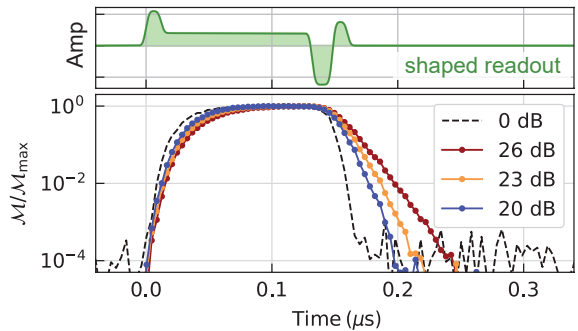


Figure S9. Slowing down of the reflected wave-packet containing the state information of the qubit after passing through the SPA. The normalized reflected readout signal is plotted against time when the SPA is biased to produce different gain. A higher gain, makes the bandwidth narrower causing a more significant delay.

optimization problem:

$$\begin{aligned} \underset{\{A_i, l_i, \Delta_0\} \in \mathbb{R}}{\text{minimize}} \quad & \vartheta(A_i, l_i, \Delta_0), \quad \ni |\alpha_g|^2, |\alpha_e|^2 < \bar{n}_{\text{max}} \\ & \text{and } A_i \neq 0, \text{ and } \sum_i l_i = \tau_{\text{ro}} \end{aligned} \quad (\text{S25})$$

$$\vartheta(A_i, l_i, \Delta_0) = \frac{\int_{\tau_{\text{ro}}}^{\infty} |\alpha_g(t) - \alpha_e(t)|^2 dt}{\int_0^{\tau_{\text{ro}}} |\alpha_g(t) - \alpha_e(t)|^2 dt},$$

By allowing the pulse detuning (Δ_0) to be a free parameter, we can compensate to the leading order the asymmetry due to the resonator non-linearity for small K .

C. Delay caused by the SPA

At the chosen operation point that provides 26 dB gain, the SNAIL parametric amplifier (SPA) in our setup has a relatively smaller bandwidth, 8 MHz, compared to the readout resonator. This causes slowing down of the readout wave-packet emitted from the resonator. To calibrate and reliably assess the performance of the shaped pulse, therefore, we turn off the SPA and perform 100 000 shots of measurements to achieve sufficient SNR. We show this with the back dashed curve in Fig. S9, by plotting the normalized measurement rate (M/M_{max}) vs time for the entire duration of the pulse and afterwards. We then tune the SPA to different gain settings ranging from 20 dB to 26 dB and show that as the gain increases, the SPA bandwidth is reduced, thus increasing the slowdown (shown with blue, yellow and dark red traces, respectively, averaged over 20 000 shots). Thus to capture the entire wave-packet and acquire the complete information, one needs to integrate longer than the readout duration itself. This highlights the need for broadband parametric amplifiers in the readout amplification chain for our future experiments to carry out fast measurements.

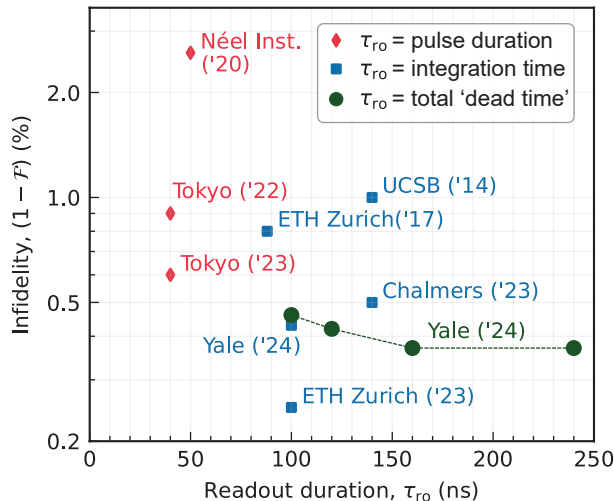


Figure S10. State of the art readout fidelity and readout duration. Different colors and symbols represent different definitions used to report the “readout duration”. The red diamonds represent the references where it refers to the time-span of the applied readout pulse, and the blue squares represent those where it is defined as the integration time. In this work, we have defined the readout duration that includes the resonator ramp-up and ramp-down times and the corresponding data is shown by green circles. For comparison, we have also reported our result in terms of integration time, with one data point at 100 ns. Note that, Chalmers (‘23)[15] uses excited state promotion techniques.

V. REVIEW OF OTHER DISPERSIVE READOUTS AND PURCELL FILTERS

We compare the readout performance and the qubit relaxation time in our experiments with other related works reported before us. In Table S2 we list the choice of readout parameters such as the external coupling of the readout resonator (κ_r), dispersive interaction between the qubit and the readout resonator (χ_{qr}) and the *undriven* relaxation time (T_1) of the qubit.

References	Parameters	$\kappa_r/2\pi$ (MHz)	$\chi_{qr}/2\pi$ (MHz)	Undriven T_1 (μ s)
USCB [†] , 2014 [11]		4.3	N.A.	11
TU Delft, 2016 [12]		0.62	-2.6	25
ETH, 2017 [13]		37.5	-15.8	7.6
Institut Néel, 2020 [14]		12.1	-9.0	3.3
Tokyo, 2022 [7]		45.7	-6.9	17
Chalmers, 2023 [15]		11	-12.6	6.2
Tokyo, 2023 [16]		11.8	-11.8	17
ETH, 2023 [17]		25.0	-6.3	30.
This work, 2024		11.6	-6.4	50.

Table S2. Cavity line-width, dispersive interaction and idle device T_1 , when there is no photons in the readout cavity, for the references in Fig. S10. [†]Information about dispersive interaction strength χ is not provided in the reference.

In Fig. S10, we list the reported readout duration and the readout infidelity in superconducting circuits. However, for the lack of unified convention to define the readout speed, we use different color and markers to label the experiments numbers. The red diamonds, represent the experiments stating readout pulse duration and the blue squares refer to the experiments where the readout duration is defined with respect to the integration time. Here, we introduce a stricter definition (shown by the green circles) to account for the resonator ramp-up and ramp-down times within the readout duration.

VI. READOUT-INDUCED STATE TRANSITIONS

The measurement rate during the readout operation is proportional to the intra-resonator photon number \bar{n}_r . Thus ideally using higher readout power leads to higher SNR in a shorter readout duration. However, generally a higher readout power causes detrimental state transitions that degrades the readout performance. We investigate the rate of these transitions on our device as a function of readout power.

We first initialize the dimon either in the $|0_q0_m\rangle$ state or in the $|1_q0_m\rangle$ state. Then we populate the readout resonator with a stimulation tone for a variable amount of time and amplitude, measured in terms of the ac Stark shift on the qubit $\Delta_q^{ac}/2\pi$. The stimulation tone is parked at a frequency, $(\omega_r^{(0_q0_m)} - \chi_{qr}/2)$, i.e. the readout frequency corresponding to maximized phase separation under low power. After evacuating the resonator, we apply a 1μ s long low power readout pulse to readout the population after the stimulation drive, as shown in Fig. S11. This readout is optimized to well discriminate $|0_q0_m\rangle$, $|1_q0_m\rangle$ and other states, with minimal state transitions induced by the readout itself.

Under a drive strength corresponding to qubit Stark shift below 50 MHz, the dominant detrimental effect is an enhanced decay rate. At a higher drive strength, however, transitions into leakage states become prominent. In this appendix, we discuss these two distinct types of readout-induced state transitions: the decay events and leakage events.

A. Readout-induced decay

The histograms shown in main text Fig. 3 suggest that the majority of our readout infidelity arises from the $P(0|e)$ error, which is dominated by qubit decay. Ideally, shorter readout duration should help against infidelity arising from the decay during readout. However, we don’t observe such improvements, and the typical error magnitude $P(0|e) > 1.5\%$ within the readout duration of 100 ns to 240 ns is not accounted for by the bare qubit

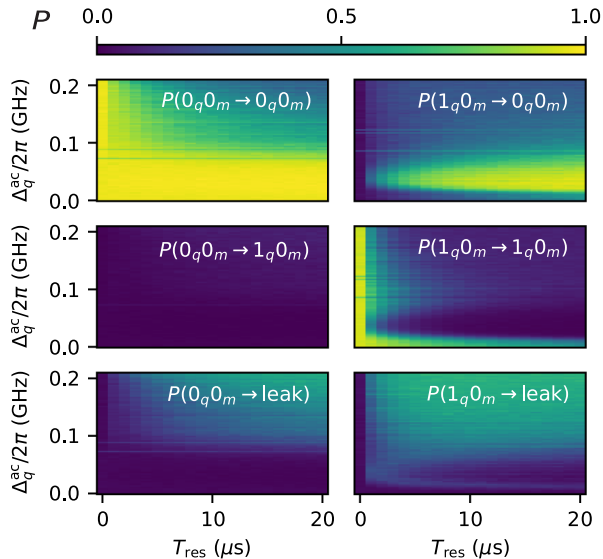


Figure S11. Readout-induced state transition under sweeping readout drive strength (calibrated by qubit Stark shift) and resonator population time, for system initialized in qubit g and e states. The readout drive causes both Pauli errors (e to g decay) and leakage errors (transition into non-computational states).

T_1 of 50 μs . This results from an enhanced qubit decay rate as a function of readout drive strength, as illustrated in Fig. S11 (right panel). What causes this degradation?

Under the readout drive, the qubit transition frequency is ac Stark shifted and broadened due to dephasing. To investigate how the readout drive modifies the T_1 of the qubit mode and its relation with the dissipation spectrum near the qubit frequency we interleave two experiments. We monitor the qubit energy relaxation time in presence of (a) an off-resonant and (b) a resonant CW drive of varying amplitude. The drive strengths are calibrated respectively into the mean ac Stark shift they impose on the qubit. The off-resonant drive is detuned by +70 MHz from the readout resonator, Stark shifting the qubit without dephasing. The qubit decay rate as a function of the ac Stark shift represents the dissipation spectrum below the undriven qubit frequency. Under a resonant drive at readout frequency, the qubit decay rate is a convolution of the dissipation spectrum and the broadened qubit line-width due to dephasing[18].

We observe that the qubit T_1 drops to below 10 μs when Stark shifted into a few ‘hot spots’ in the dissipation spectrum from the experiment with off-resonant drive, as shown in Fig. S12 (left panel). These ‘hot spots’ exhibit drifts on the order of MHz over hours. They are believed to originate primarily from dielectric two-level systems (TLS), that has been long acknowledged as a leading energy relaxation channel of superconducting qubits[19–21]. Similar temporal fluctuations due to TLS

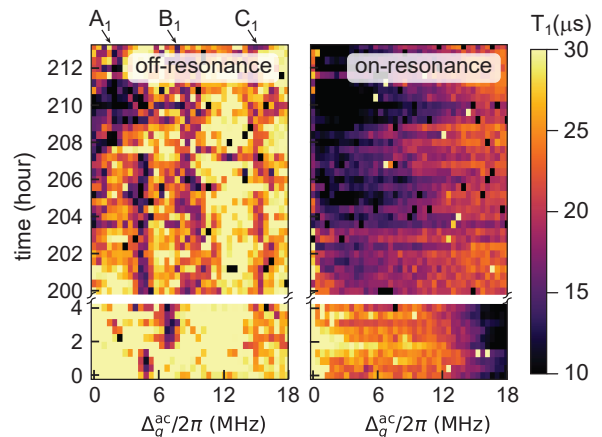


Figure S12. Qubit energy relaxation time (T_1) under off-resonance (left panel) and on-resonance (right panel) drives. The off-resonance drive is detuned from the readout frequency, inducing only a Stark shift, while the on-resonance drive applied at the readout frequency, causes both a Stark shift and dephasing. In the left panel, the qubit T_1 exhibits significant degradation when Stark-shifted into ‘hot spots’ in the dissipation spectrum, which drift over time. The right panel demonstrates the combined effect of the dissipation spectrum and the anti-Zeno effect on the qubit T_1 when subjected to a readout drive.

frequency drifting have also been reported in previous works[22, 23].

We observe that qubit T_1 dependence on readout (resonant) drive strength varies significantly based on the TLS distribution in the spectrum. The driven T_1 is expected to degrade due to ‘hot spots’ away from the qubit frequency via the anti-Zeno effect. As an example, see Fig. S12 for the time 0 - 4 hours. On the other hand, when having nearby TLS(s), stronger drive can improve T_1 through the Zeno effect [18] (207 - 211 hours in Fig. S12). As a result, the temporal variation of $T_1(\bar{n}_c)$ causes noticeable variation to the optimal readout fidelity for $|e\rangle$ state across days. The fluctuation of $|e\rangle$ readout infidelity has been reported as a major challenge for the long-time stability of system calibration[23].

B. Readout-induced leakage

As we move to higher readout powers, the transitions into non-computational states become dominant, as shown in Fig. S11. We also observe that the $|1_q 0_m\rangle$ state starts to show transitions into leakage states at a lower drive strength and also with a faster rate, compared to the $|0_q 0_m\rangle$ state. Compared to the readout-induced decay that leads to Pauli errors, the readout-induced leakage errors are more harmful in applications where repeated readouts are required. Such readout-induced leakage events are generally present in superconducting

circuits[24–26], imposing an ultimately limit on the readout performance.

The mechanisms behind readout-induced leakage is an active topic of research. Several recent theory works[27, 28] identifies the multi-photon excitation activated by the readout drive $\xi^i(\hat{a}_q^\dagger)^j$ as the leading cause for such transitions in transmon. The symmetry of the Josephson potential guarantees that only transitions with $(i+j) = 0 \pmod{2}$ are allowed. In dimon the readout drive can cause simultaneous excitation involving the qubit and mediator modes, in addition to the individual excitation of each mode. This significantly increases the density of such transitions in the frequency space of the drive. However, the 2D non-linear potential (in Eq. S4) combined with the fact that the readout drive is linearly uncoupled from the qubit mode modifies the selection rule. As a result, only transitions $\xi^i(\hat{a}_m^\dagger)^j(\hat{a}_q^\dagger)^k$ with $(i+j) = 0 \pmod{2}$ and $k = 0 \pmod{2}$ are allowed.

VII. PSEUDO-SYNDROME DETECTION TECHNIQUE

The pseudo-syndrome detection experiment consists of the following steps.

1. Choose the sequence length M that indicates the total number of cycles in the pseudo-syndrome detection. In our experiment, each random sequence of the pseudo-syndrome detection experiment consists of $M = 40$ readout operations after a pre-selection readout that prepares the qubit in $|g\rangle$ with fidelity above 99.9%.
2. Construct K different randomizations for the input bit-string and generate the corresponding sequences $\mathcal{R}_0 \circ \left(\prod_{m=1}^M \mathcal{P}_m \circ \mathcal{R}_m \right)$, where $\mathcal{P}_m \in \{X, I\}$ is determined by the input bit-string $\{i_m\}$, and \mathcal{R}_m is the m -th readout operation.
3. From the neighbouring pairs of readout outcomes r_m and r_{m-1} , construct the output “flipped-or-not” bit-string $\{o_m\}$ such that $o_m \equiv r_{m-1} \oplus r_m$, where \oplus represents the XOR operation on the two bits. Ideally, it should be identical to the input “X-or-I” bit-string.
4. Compute the bit-wise correlation, $C_m = 1 - 2(i_m \oplus o_m)$ for each experimental realization of the sequence, where $C_m \in \{-1, +1\}$.
5. Perform N experimental realizations to compute the average bit-wise correlation, \bar{C}_m for each random sequence. In our experiments, we keep 9000 post-selected shots after discarding the shots with erroneous state preparation.

6. Average over different randomizations to obtain the mean success probability $\langle \bar{C} \rangle_m$ for syndrome detection. In the data presented here, we have averaged over 98 random input strings.

In the following, we provide details of the data processing, and provide a theoretical model to extract the leakage rate from the experimental data.

A. Output bit-string processing

To illustrate our protocol, we use an example and show the readout outcomes for the calibrated pulse at $\bar{n}_r = 7.6$ for three special input bit-strings: $I^{\otimes M}$, $I^{\otimes(M-1)}X$ and $X^{\otimes M}$ in Fig. S13(a-c) (red and blue). We also show the inferred output bit-string (dark green and grey). Ideally, they correspond to 40 readouts on the $|g\rangle$ states, 40 readouts on the $|e\rangle$ states, and 40 readouts with the qubit flipped between each pair of readouts. Finally we show an example of a random input sequence in Fig. S13(d), emulating the inputs from syndrome detection cycles in QEC. From the readout outcomes and the inferred output bit-strings in Fig. S13(a-d), we observe three distinct types of error affecting the readout:

1. A discrimination error (due to finite SNR) corrupts one individual readout outcome, leading to two neighbouring output bits to be anti-correlated to the input bits.
2. A Pauli error, i.e. a $|g\rangle \rightarrow |e\rangle$ heating, or an $|e\rangle \rightarrow |g\rangle$ decay still keeps the qubit in the computational subspace leading to only one output bit to be anti-correlated.
3. A leakage error leaves the bit-flip operations ineffective, making all the following output bits corrupted.

Only the third kind of error accumulates and results in an exponential decay in the correlation of the input and the output bit-strings.

In the limiting case of $P(1|\psi_l) = 1$ (or $P(0|\psi_l) = 1$), as the qubit remains in the leakage states the readout outcomes remain fixed at ‘1’ irrespective of the input operations. Thus the output bit will appear anti-correlated when the input operation is ‘X’ and correlated when the input operation is ‘I’. When a random input bit string is chosen, the bit-wise correlation \bar{C}_m (averaged over N experimental realizations) either is close to 1 (when $i_m = I$), or decays exponentially with m (when $i_m = X$). In the other limiting case of $P(0|\psi_l) = P(1|\psi_l) = 1/2$, when the qubit is in the leakage states the readout outcomes are fully randomized. Thus, irrespective of the input operations ($i_m = X$ or I) \bar{C}_m will follow the same exponential decay curves.

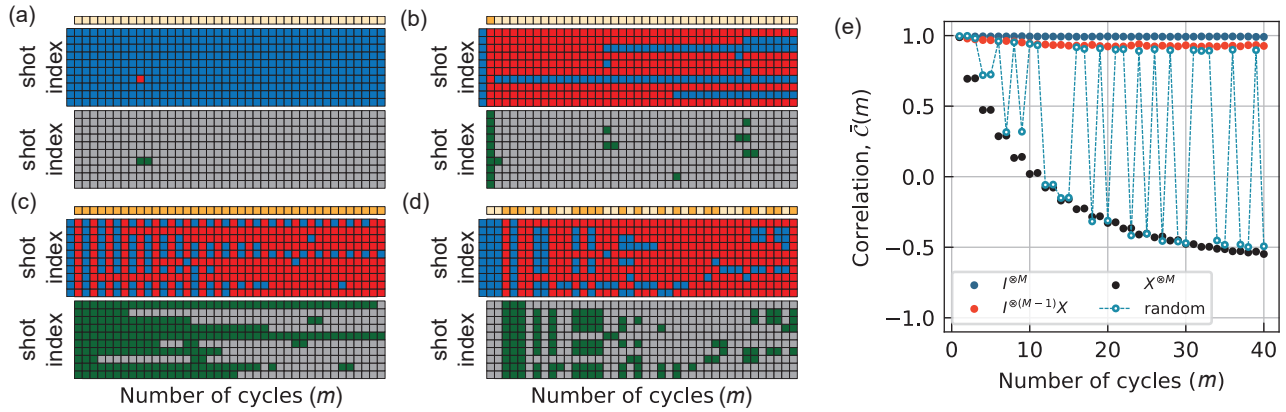


Figure S13. Example of pseudo-syndrome detection decoding for a readout pulse corresponding to $\bar{n}_r = 7.6$ for different inputs: (a) $I^{\otimes M}$, (b) $I^{\otimes(M-1)}X$, (c) $X^{\otimes M}$ and (d) a randomized sequence. Top row: input sequence $\{i_m\}$ (orange for X , off-white for I). Middle panel: 10 example sequences of the readout outcomes (blue for 0, red for 1). Bottom panel: corresponding output bit-string $\{o_m\}$ (green for “flipped”, grey for “not-flipped”). (e) Bit-wise correlation between $\{o_m\}$ and $\{i_m\}$ averaged over 9000 shots for the four example inputs.

In our experiment $P(1|\psi_l) \sim 1$, that results in \bar{C}_m sampling between two distributions following the $I^{\otimes(M-1)}X$ and $X^{\otimes M}$ curves dependent on the input operations, as shown in Fig. S13(e). We apply 98 different randomizations of input sequence $\{i_m\}$ to obtain the mean success probability $\langle \bar{C}_m \rangle$ of the syndrome detection, plotted in Fig. S14(a-d) for four different readout powers. In addition, we also post-select the shots where $i_m = I$ (or $i_m = X$) and plot the mean correlation for these two classes. The difference between them is representative of the imbalance between $P(1|\psi_l)$ and $P(0|\psi_l)$. The error bar of $\langle \bar{C}_m \rangle$ is the average of the standard deviation of the two distributions.

B. Leakage models

We assume a simplified model to fit the experimental data in pseudo-syndrome detection and estimate a rate for the readout-induced leakage. We consider a larger Hilbert space consisting of the $d_1 = 2$ -dimensional computational subspace \mathcal{X}_1 , and a d_2 -dimensional leakage subspace \mathcal{X}_2 , with $\mathbb{1}_1$ and $\mathbb{1}_2$ being the projectors onto the respective subspaces[29]. Thus the full dynamics happen in a $(d_1 + d_2)$ -dimensional direct-sum state space $\mathcal{X}_1 \oplus \mathcal{X}_2$. Let ρ be an arbitrary state defined in the $(d_1 + d_2)$ dimensional Hilbert space. The total leakage population of state ρ is then defined as $\mathfrak{L}(\rho) = \text{Tr}[\mathbb{1}_2 \rho]$. We can describe the leakage error channel for a single cycle of pseudo-syndrome detection as a completely positive trace preserving (CPTP) map, \mathcal{E}_L in this $(d_1 + d_2)$ dimensional space. Therefore, if we initiate the system in a given state $|\psi\rangle$ within the computational subspace, the leakage rate for one cycle is given by: $p_l = \mathfrak{L}(\mathcal{E}_L[|\psi\rangle\langle\psi_1|])$. However, instead of focusing on the leakage rate from a particular state, we are rather interested in the average leakage rate

L_\uparrow of the channel \mathcal{E}_L when acted on a random input state in the computational subspace:

$$L_\uparrow(\mathcal{E}_L) = \int d\psi_l \mathfrak{L}(\mathcal{E}_L[|\psi_l\rangle\langle\psi_l|]) = \mathfrak{L}\left(\mathcal{E}_L\left(\frac{\mathbb{1}_1}{d_1}\right)\right) \quad (\text{S26})$$

Note that we can still put a bound on the worst case leakage from any individual state ρ' in the computational subspace (assuming all the leakage happens from that state):

$$\mathfrak{L}_{\max}(\mathcal{E}_L[\rho_0]) \leq d_1 L_\uparrow(\mathcal{E}_L). \quad (\text{S27})$$

In the same spirit, we can also define an average *seepage* rate, the rate at which the population may decay back into the computational subspace, caused by the error channel by averaging over all leakage states $|\psi_l\rangle$:

$$L_\downarrow(\mathcal{E}_L) = 1 - \int d\psi_l \mathfrak{L}(\mathcal{E}_L[|\psi_l\rangle\langle\psi_l|]) = 1 - \mathfrak{L}\left(\mathcal{E}_L\left(\frac{\mathbb{1}_2}{d_2}\right)\right), \quad (\text{S28})$$

To describe the leakage process, we assume that there is no coherent exchange between the computation states and the leakage states. We define a completely depolarizing channel $\mathcal{D}_{ij}(\rho)$ between subspaces \mathcal{X}_i and \mathcal{X}_j :

$$\mathcal{D}_{ij}(\rho) = \text{Tr}[\mathbb{1}_j \rho] \frac{\mathbb{1}_i}{d_i}, \quad i, j \in \{1, 2\} \quad (\text{S29})$$

\mathcal{D}_{12} and \mathcal{D}_{21} destroys any coherence in the leakage and seepage process and \mathcal{D}_{22} destroys any coherent dynamics in the leakage subspace. This is an important *assumption* that eliminates any memory effects to arrive at an exponential decay model.

The leakage error can then be described as a completely positive trace preserving (CPTP) map, \mathcal{E}_L :

$$\mathcal{E}_L = (1 - L_\uparrow)\mathcal{E}_1 + L_\uparrow\mathcal{D}_{21} + L_\downarrow\mathcal{D}_{12} + (1 - L_\downarrow)\mathcal{D}_{22}, \quad (\text{S30})$$

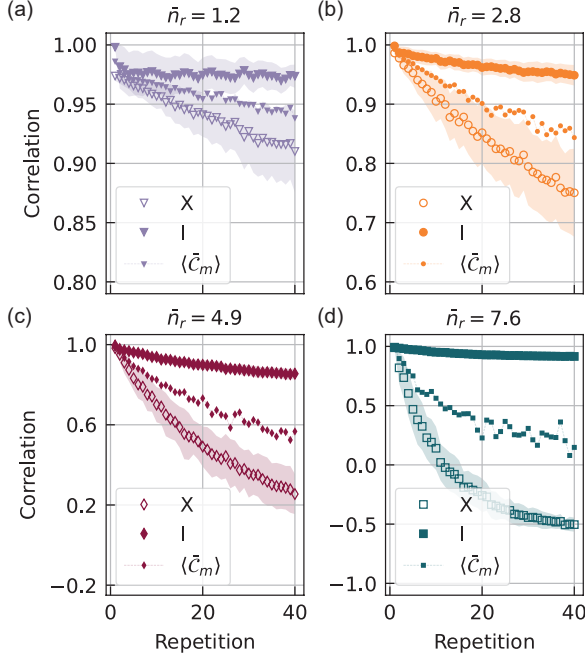


Figure S14. Decay of correlation. Additional fluctuation in the mean correlation is due to finite sampling and the deviation of p_{\times} from 0.5.

where \mathcal{E}_1 , in general, is an arbitrary CPTP map within the computational subspace. The readout operation combined with the randomized bit-flips turns it into a completely depolarizing channel, \mathcal{D}_{11} that may also absorb any Pauli error.

We can compute the leakage population after m applications of the pseudo-syndrome cycle by raising the error channel \mathcal{E}_L to power m : (Does it hold without knowing the measurement outcome).

$$\mathfrak{L}(\mathcal{E}_L^m[\rho]) = \text{Tr}[\mathbb{1}_2 \mathcal{E}_L^m[\rho]] = \text{Tr}\left[\rho \left(\mathcal{E}_L^\dagger\right)^m [\mathbb{1}_2]\right] \quad (\text{S31})$$

To arrive at the last expression, we have used the properties of matrix adjugates, $\text{Tr}[A] = \text{Tr}[A^\dagger]$ and $(AB)^\dagger = B^\dagger A^\dagger$.

As the operators \mathcal{D}_{ij} are all mutually orthogonal, we can express the superoperator for \mathcal{E}_L with respect to the bases, $|\mathbb{1}_1\rangle \equiv (1, 0)$ and $|\mathbb{1}_2\rangle \equiv (0, 1)$ by a 2×2 matrix:

$$\mathcal{S}_{\mathcal{E}_L} = \begin{pmatrix} 1 - L_\uparrow & L_\downarrow \\ L_\uparrow & 1 - L_\downarrow \end{pmatrix}, \quad (\text{S32})$$

The superoperator for the hermitian conjugate matrix (\mathcal{E}_L^\dagger) and its m -th power can be written as:

$$\begin{aligned} \mathcal{S}_{\mathcal{E}_L^\dagger} &= \begin{pmatrix} 1 - L_\uparrow & L_\uparrow \\ L_\downarrow & 1 - L_\downarrow \end{pmatrix}, \\ \mathcal{S}_{\mathcal{E}_L^m} &= \frac{1}{L} \begin{pmatrix} L_\downarrow & L_\uparrow \\ L_\downarrow & L_\uparrow \end{pmatrix} + \frac{(1-L)^m}{L} \begin{pmatrix} L_\uparrow & -L_\uparrow \\ -L_\downarrow & L_\downarrow \end{pmatrix} \end{aligned} \quad (\text{S33})$$

We can apply this superoperator on the basis state $|\mathbb{1}_2\rangle$ to obtain:

$$\begin{aligned} \mathcal{S}_{\mathcal{E}_L^m} |\mathbb{1}_2\rangle &= \frac{L_\uparrow}{L} (|\mathbb{1}_1\rangle + |\mathbb{1}_2\rangle) \\ &\quad - \frac{(1-L)^m}{L} (L_\uparrow |\mathbb{1}_1\rangle - L_\downarrow |\mathbb{1}_2\rangle) \end{aligned} \quad (\text{S34})$$

Hence, using Eq. S31 and Eq. S34 we find the expression the total leakage population after m application of the pseudo-syndrome cycle when start from an initial state with a leakage population p_{ini} :

$$\begin{aligned} \mathfrak{L}(\mathcal{E}_L^m[\rho]) &= \left((1 - p_{\text{ini}}) \langle \mathbb{1}_1 | + p_{\text{ini}} \langle \mathbb{1}_2 | \right) \mathcal{S}_{\mathcal{E}_L^m} |\mathbb{1}_2\rangle \\ &= \frac{L_\uparrow}{L} - (1-L)^m \left(\frac{L_\uparrow}{L} - p_{\text{ini}} \right) \end{aligned} \quad (\text{S35})$$

If the *bit-flip operation is perfect* and either $P(0|\psi_l) = 0$ or $P(1|\psi_l) = 0$ and there is *no other readout error apart from leakage*, the average bit-wise correlation between the input string and the output string is given by:

$$\begin{aligned} \langle \bar{c}_m \rangle &= \frac{(+1)}{2} + \frac{(+1)[1 - \mathfrak{L}(\mathcal{E}_L^m[\rho])] + (-1)[\mathfrak{L}(\mathcal{E}_L^m[\rho])]}{2} \\ &= 1 - \mathfrak{L}(\mathcal{E}_L^m[\rho]) = \frac{L_\downarrow}{L} - (1-L)^m \left(\frac{L_\uparrow}{L} - p_{\text{ini}} \right), \end{aligned} \quad (\text{S36})$$

And we can individually estimate L_\uparrow , L_\downarrow and p_{ini} . However, in presence of other errors such as, imperfect bit-flip operations (ϵ_π), Pauli errors (ϵ_Γ), readout discrimination error (ϵ_{SNR}), and when $0 < P(0|\psi_l) < 1$, the pre-factors get modified and they can be combined into two constants to be determined from the fit:

$$\langle \bar{c}_m \rangle = \frac{1}{2} (A + B(1-L)^m), \quad (\text{S37})$$

We use this expression to fit the experimental data and estimate the combined leakage-seepage rate L for the four readout pulses optimized for different powers.

* sumeru.hazra@yale.edu, wei.dai.wd279@yale.edu; These two authors contributed equally

† michel.devoret@yale.edu

- [1] J. M. Gambetta, A. A. Houck, and A. Blais, Phys. Rev. Lett. **106**, 030502 (2011).
- [2] J. Koch, T. M. Yu, J. Gambetta, A. A. Houck, D. I. Schuster, J. Majer, A. Blais, M. H. Devoret, S. M. Girvin, and R. J. Schoelkopf, Phys. Rev. A **76**, 042319 (2007).
- [3] R. Rehammar and S. Gasparinetti, IEEE Transactions on Microwave Theory and Techniques (2023).
- [4] X. Y. Jin, A. Kamal, A. P. Sears, T. Gudmundsen, D. Hover, J. Miloshi, R. Slattery, F. Yan, J. Yoder, T. P. Orlando, S. Gustavsson, and W. D. Oliver, Phys. Rev. Lett. **114**, 240501 (2015).

- [5] M. Mirhosseini, E. Kim, X. Zhang, A. Sipahigil, P. B. Dieterle, A. J. Keller, A. Asenjo-Garcia, D. E. Chang, and O. Painter, *Nature* **569**, 692 (2019).
- [6] Y. Lu, A. Bengtsson, J. J. Burnett, E. Wiegand, B. Suri, P. Krantz, A. F. Roudsari, A. F. Kockum, S. Gasparinetti, G. Johansson, *et al.*, *npj Quantum Information* **7**, 35 (2021).
- [7] Y. Sunada, S. Kono, J. Ilves, S. Tamate, T. Sugiyama, Y. Tabuchi, and Y. Nakamura, *Phys. Rev. Appl.* **17**, 044016 (2022).
- [8] A. A. Houck, J. A. Schreier, B. R. Johnson, J. M. Chow, J. Koch, J. M. Gambetta, D. I. Schuster, L. Frunzio, M. H. Devoret, S. M. Girvin, and R. J. Schoelkopf, *Phys. Rev. Lett.* **101**, 080502 (2008).
- [9] F. R. Ong, M. Boissonneault, F. Mallet, A. C. Doherty, A. Blais, D. Vion, D. Esteve, and P. Bertet, *Phys. Rev. Lett.* **110**, 047001 (2013).
- [10] B. Yurke and E. Buks, *Journal of Lightwave Technology* **24**, 5054 (2006).
- [11] E. Jeffrey, D. Sank, J. Y. Mutus, T. C. White, J. Kelly, R. Barends, Y. Chen, Z. Chen, B. Chiaro, A. Dunsworth, A. Megrant, P. J. J. O’Malley, C. Neill, P. Roushan, A. Vainsencher, J. Wenner, A. N. Cleland, and J. M. Martinis, *Phys. Rev. Lett.* **112**, 190504 (2014).
- [12] C. C. Bultink, M. A. Rol, T. E. O’Brien, X. Fu, B. C. S. Dikken, C. Dickel, R. F. L. Vermeulen, J. C. de Sterke, A. Bruno, R. N. Schouten, and L. DiCarlo, *Phys. Rev. Appl.* **6**, 034008 (2016).
- [13] T. Walter, P. Kurpiers, S. Gasparinetti, P. Magnard, A. Potočnik, Y. Salathé, M. Pechal, M. Mondal, M. Oppliger, C. Eichler, and A. Wallraff, *Phys. Rev. Appl.* **7**, 054020 (2017).
- [14] R. Dassonneville, T. Ramos, V. Milchakov, L. Planat, E. Dumur, F. Foroughi, J. Puertas, S. Leger, K. Bharadwaj, J. Delaforce, C. Naud, W. Hasch-Guichard, J. J. García-Ripoll, N. Roch, and O. Buisson, *Phys. Rev. X* **10**, 011045 (2020).
- [15] L. Chen, H.-X. Li, Y. Lu, C. W. Warren, C. J. Križan, S. Kosen, M. Rommel, S. Ahmed, A. Osman, J. Biznárová, *et al.*, *npj Quantum Information* **9**, 26 (2023).
- [16] Y. Sunada, K. Yuki, Z. Wang, T. Miyamura, J. Ilves, K. Matsuura, P. A. Spring, S. Tamate, S. Kono, and Y. Nakamura, *PRX Quantum* **5**, 010307 (2024).
- [17] F. Swiadek, R. Shillito, P. Magnard, A. Remm, C. Hellings, N. Lacroix, Q. Ficheux, D. C. Zanuz, G. J. Norris, A. Blais, S. Krinner, and A. Wallraff, “Enhancing dispersive readout of superconducting qubits through dynamic control of the dispersive shift: Experiment and theory,” (2023), arXiv:2307.07765 [quant-ph].
- [18] T. Thorbeck, Z. Xiao, A. Kamal, and L. C. G. Govia, *Phys. Rev. Lett.* **132**, 090602 (2024).
- [19] J. M. Martinis, K. B. Cooper, R. McDermott, M. Steffen, M. Ansmann, K. D. Osborn, K. Cicak, S. Oh, D. P. Pappas, R. W. Simmonds, and C. C. Yu, *Phys. Rev. Lett.* **95**, 210503 (2005).
- [20] J. M. Gambetta, C. E. Murray, Y.-K.-K. Fung, D. T. McClure, O. Dial, W. Shanks, J. W. Sleight, and M. Steffen, *IEEE Transactions on Applied Superconductivity* **27**, 1 (2017).
- [21] C. Wang, C. Axline, Y. Y. Gao, T. Brecht, Y. Chu, L. Frunzio, M. Devoret, and R. J. Schoelkopf, *Applied Physics Letters* **107** (2015).
- [22] P. V. Klimov, J. Kelly, Z. Chen, M. Neeley, A. Megrant, B. Burkett, R. Barends, K. Arya, B. Chiaro, Y. Chen, A. Dunsworth, A. Fowler, B. Foxen, C. Gidney, M. Giustina, R. Graff, T. Huang, E. Jeffrey, E. Lucero, J. Y. Mutus, O. Naaman, C. Neill, C. Quintana, P. Roushan, D. Sank, A. Vainsencher, J. Wenner, T. C. White, S. Boixo, R. Babbush, V. N. Smelyanskiy, H. Neven, and J. M. Martinis, *Phys. Rev. Lett.* **121**, 090502 (2018).
- [23] V. Sivak, A. Eickbusch, B. Royer, S. Singh, I. Tsioutsios, S. Ganjam, A. Miano, B. Brock, A. Ding, L. Frunzio, *et al.*, *Nature* **616**, 50 (2023).
- [24] D. Sank, Z. Chen, M. Khezri, J. Kelly, R. Barends, B. Campbell, Y. Chen, B. Chiaro, A. Dunsworth, A. Fowler, E. Jeffrey, E. Lucero, A. Megrant, J. Mutus, M. Neeley, C. Neill, P. J. J. O’Malley, C. Quintana, P. Roushan, A. Vainsencher, T. White, J. Wenner, A. N. Korotkov, and J. M. Martinis, *Phys. Rev. Lett.* **117**, 190503 (2016).
- [25] M. Khezri, A. Opremca, Z. Chen, K. C. Miao, M. McEwen, A. Bengtsson, T. White, O. Naaman, D. Sank, A. N. Korotkov, Y. Chen, and V. Smelyanskiy, *Phys. Rev. Appl.* **20**, 054008 (2023).
- [26] Y. Hirasaki, S. Daimon, N. Kanazawa, T. Itoko, M. Tokunari, and E. Saitoh, arXiv preprint arXiv:2402.05409 (2024).
- [27] X. Xiao, J. Venkatraman, R. G. Cortiñas, S. Chowdhury, and M. H. Devoret, “A diagrammatic method to compute the effective hamiltonian of driven nonlinear oscillators,” (2023), arXiv:2304.13656.
- [28] M. F. Dumas, B. Groleau-Paré, A. McDonald, M. H. Muñoz-Arias, C. Lledó, B. D’Anjou, and A. Blais, arXiv preprint arXiv:2402.06615 (2024).
- [29] C. J. Wood and J. M. Gambetta, *Phys. Rev. A* **97**, 032306 (2018).